RESEARCH ARTICLE

Key Points:
- Shear bands in the South Armorican Shear Zone record changes in dominant deformation mechanisms
- Initiation by microcracking and early evolution via dislocation and dissolution-precipitation creep
- Shear bands document nonsteady state mechanical evolution of the brittle-ductile transition

Correspondence to:
Z. Bukovská,
zita.bukovska@geology.cz

Major softening at brittle-ductile transition due to interplay between chemical and deformation processes: An insight from evolution of shear bands in the South Armorican Shear Zone

Zita Bukovská[1,2], Petr Jeřábek[1], and Luiz F. G. Morales[3]

[1]Institute of Petrology and Structural Geology, Charles University in Prague, Prague, Czech Republic, [2]Czech Geological Survey, Prague, Czech Republic, [3]Helmholtz Centre Potsdam, German Research Centre GFZ, Potsdam, Germany

Abstract The formation of S-C/C′ fabrics in the South Armorican Shear Zone has been evaluated by detailed microstructural study where the focus was given to initiation and early evolution of the C/C′ fabric shear bands. Our observations suggest that the S-C/C′ fabrics formed at distinct temperature conditions indicating >550°C for the S fabric and 300–350°C at 100–400 MPa for the C/C′ fabric shear bands. The evolving microstructure within shear bands documents switches in deformation mechanisms related to positive feedbacks between deformation and chemical processes and imposes mechanical constraints on the evolution of the brittle-ductile transition in the continental transform fault domains. Three stages of shear band evolution have been identified. Stage I corresponds to initiation of shear bands via formation of microcracks with possible yielding differential stress of up to 250 MPa. Stage II is associated with subgrain rotation recrystallization and dislocation creep of quartz and coeval dissolution-precipitation creep of microcline. Recrystallized quartz grains show continual increase in size and decrease in stress and strain rates from 94 MPa to 17–26 MPa and $1.8 \times 10^{-1}\,s^{-1}$–$9 \times 10^{-17}\,s^{-1}$ associated with deformation partitioning into weaker microcline layer and shear band widening. The quartz mechanical data allowed us to set some constrains for coeval dissolution-precipitation of microcline which at our estimated pressure-temperature conditions suggests creep at 17–26 MPa differential stress and $1.8 \times 10^{-15}\,s^{-1}$ strain rate. Stage III is characterized by localized slip along white mica bands accommodated by dislocation creep at strain rate $1.8 \times 10^{-14}\,s^{-1}$ and stress 5.75 MPa. Our mechanical data point to dynamic evolution of the studied brittle-ductile transition characterized by major weakening to strengths >10 MPa. Such nonsteady state evolution may be common in crustal shear zones especially when phase transformations are involved.

1. Introduction

Zones of intense deformation such as faults and shear zones are an expression of strain localization [e.g., *White et al.*, 1980; *Schmid*, 1982; *Rutter et al.*, 2001; *Gueydan et al.*, 2003, 2004; *Montési*, 2007]. The phenomenon of localization has been recognized across the entire lithosphere [e.g., *Karato*, 1983; *Wilks and Carter*, 1990; *Crider and Peacock*, 2004]; thus, the overall rheological response of the lithosphere to applied stress is strongly influenced by this process [*Rutter*, 1999; *Bercovici*, 2003]. It is generally accepted that deformation is more distributed with increasing depth and temperature which, in the context of the lithosphere compositional stratification, implies several vertically alternating layers of either localized or distributed deformation [e.g., *Platt and Behr*, 2011]. In contrast, recent studies demonstrated that highly localized deformation can be maintained under conditions of presumed distributed deformation [e.g., *Chopin et al.*, 2012; *Menegon et al.*, 2013; *Okudaira et al.*, 2015]. In simple terms, the maintenance of localized shear in ultramylonites demonstrates high strength contrast between the weaker shear zone and stronger wall rock, whereas the two strengths must be comparable in the case of distributed shear in mylonites [*Platt and Behr*, 2011]. The maintenance of localized shear will thus lead to an underestimation of the integral lithospheric strength. Recently, numerous small-scale studies have concentrated on rheological aspects of initiation and evolution of shear zones mainly in quartzofeldspathic rocks [*Pennacchioni and Mancktelow*, 2007; *Oliot et al.*, 2010; *Kilian et al.*, 2011; *Chopin et al.*, 2012; *Goncalves et al.*, 2012; *Menegon et al.*, 2013; *Oliot et al.*, 2014]. The initiation of shear zones is controlled by mechanical yielding of a rock [*Ranalli*, 1987] while their subsequent evolution is controlled by grain-scale processes which reflect complex interaction between metamorphism, metasomatism, and deformation so typical for natural shear zones [*Keller et al.*, 2004; *Jeřábek et al.*, 2007; *Oliot et al.*, 2010; *Goncalves et al.*, 2012].
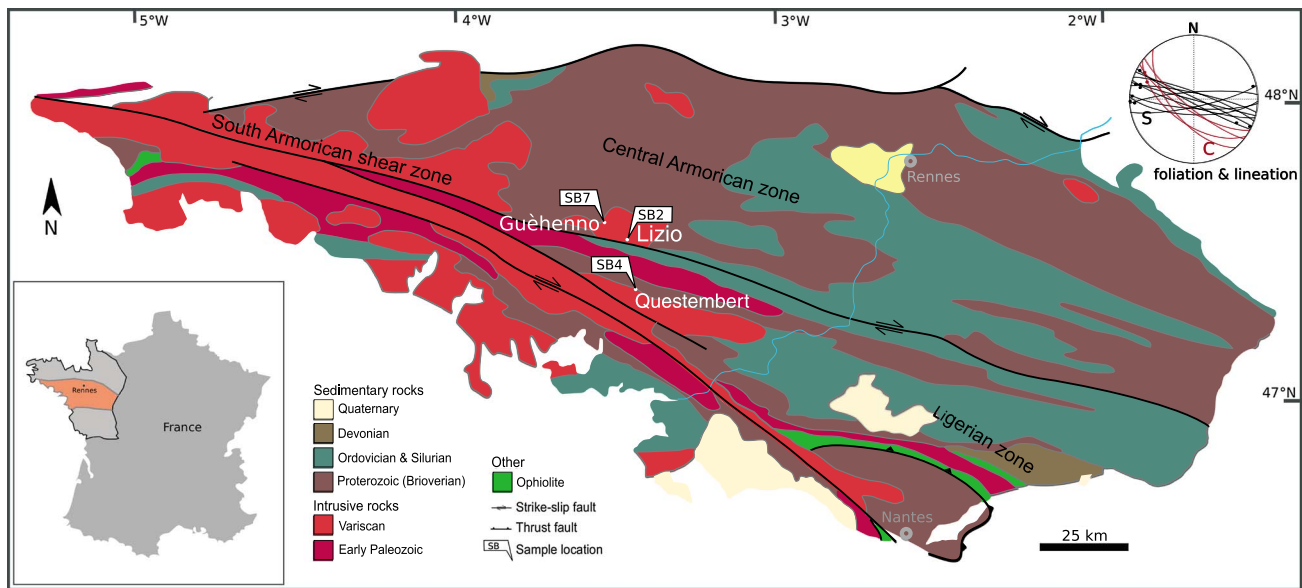
Figure 1. Simplified geological map of the studied area with location of the studied samples (map modified from Wikimedia Commons, GNU Free Documentation License). The measured orientation of S and C fabrics is shown in the equal area lower hemisphere pole figure. The black and red dots in the pole figure show the orientation of respective lineations.

Small-scale shear zones, called shear bands, C and C' fabrics, or extensional crenulation cleavage, crosscutting a metamorphic foliation at gentle to moderate angles are frequent phenomenon in major shear zones [*Berthé et al.*, 1979a, 1979b; *Platt and Vissers*, 1980; *White et al.*, 1980; *Gapais and White*, 1982; *Platt*, 1984]. These extensively studied deformation structures clearly indicate localization of deformation associated with (1) preexisting fractures or discontinuities [e.g., *Means*, 1995; *Fusseis and Handy*, 2008], (2) strain partitioning [*Krohe*, 1990; *Passchier*, 1991], or (3) reaction softening [*Stünitz and Tullis*, 2001]. In contrast to recent studies on standard shear zones, most of the studies of shear bands focused on their initiation and geometry and not on their subsequent evolution.

In this study, we present detailed microscale characterization of initiation and early evolution of shear bands in granitoids from the type locality in the major transform boundary South Armorican Shear Zone [*Berthé et al.*, 1979a, 1979b]. The quantitative analyses of microstructure, texture, and chemistry of minerals from the studied shear bands revealed the effects of positive feedback between deformation and chemical processes resulting into switches in dominant deformation mechanism and consequently to dramatic weakening of this large-scale shear zone. The pressure-temperature, stress, and strain rate estimates from the shear bands allowed us to set some mechanical constraints on the localization and early evolution of deformation in the conditions of brittle-ductile transition pointing to dynamic rheology and switches between localized and distributed deformation behavior.

2. Sample Localization and Description

South Armorican Shear Zone (SASZ) in European Variscides represents a major tectonic zone separating Central Armorican and South Armorican Massif in France [e.g., *Ballèvre et al.,* 2009; *Gumiaux et al.,* 2004]. The subvertical shear zone has approximately WSW-ENE strike with similar branches extending over several hundreds of kilometers from westernmost Brittany to Vendée-Poitou region (Figure 1). In the studied area, the shear zone affects Variscan and Early Paleozoic intrusive rocks emplaced to 3–12 km depth (338–329 Ma) [*Tartèse and Boulvais*, 2010; *Tartèse et al.*, 2012] and can be traced also into the sedimentary cover. The SASZ is right-lateral shear zone with a steep foliation and horizontal to subhorizontal lineation showing approximately 40 km of displacement in its northern branch [*Gumiaux et al.*, 2004]. The shear zone shows the development of structures called C-S or S-C fabrics which were originally described from Plumelec and Gorvello massif by *Berthé et al.* [1979a, 1979b]. It has been suggested that the shear deformation in the SASZ records an evolution from ductile to brittle conditions and occurred at 315–300 Ma [*Tartèse et al.*, 2012].
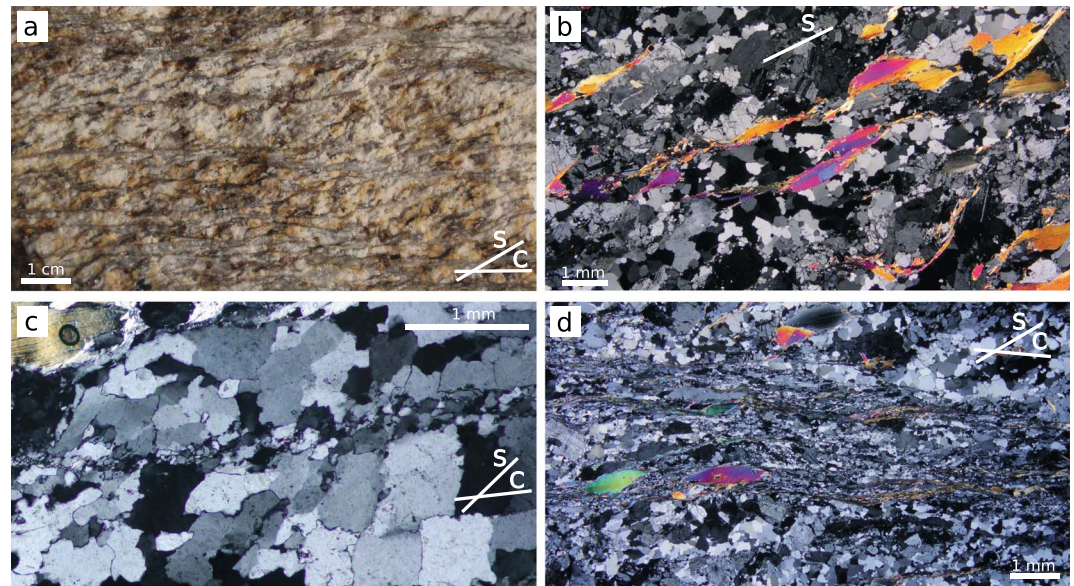
Figure 2. (a) Macrophotograph of orthogneiss sample SB4H showing S-C fabric geometry. (b) Microphotograph of S fabric defined by porphyroclasts of K-feldspar, plagioclase, white mica, and recrystallized quartz aggregates (sample SB4H, crossed polarizers). (c) Microphotograph of thin shear band crosscutting the quartz aggregate (sample SB4H, crossed polarizers). (d) Microphotograph of well-developed shear band reworking the original S fabric (sample SB4H, crossed polarizers). General orientation of S and C fabrics for each image is indicated by white lines.

The studied orthogneisses to ultramylonites formed from Variscan white mica granites. The studied samples were collected from quarries situated within the SASZ (Figure 1) with the aim to cover different stages of shear band evolution marked by increasing strain. The studied samples were collected from Lizio granite in the Plumelec abandoned quarry (Figure 1, SB2; original locality of *Berthé et al.* [1979a, 1979b], from Questembert granite in the Lescastel quarry (SB4) and from the Guéhenno granite in the Pasdrun abandoned quarry (SB7) (Figure 1).

The studied S-C fabrics (Figure 2a) comprise metamorphic foliation (S fabric) which is crosscut by shear bands (C fabric). Macroscopically, the S fabric is defined by shape-preferred orientation of quartz aggregates and porphyroclasts of K-feldspar, white mica, and plagioclase. The S fabric bears stretching lineation defined by shape of quartz aggregates. The C fabric is characterized by discrete zones occupied by fine-grained mixture of phases. The C fabric bears mineral lineation defined by spatial arrangement of small white mica grains. The shear bands show regular spacing, and the distance between individual shear surfaces decreases with increasing intensity of shear band overprint (Figures 2a and 3). Both S and C fabrics are steep, generally E-W trending in case of S fabric and NW-SE trending in case of C fabric (Figure 1). The lineations on both fabrics are horizontal to subhorizontal. The studied thin sections were cut perpendicular to both S and C fabrics and their intersection, as well as parallel to both (S and C) lineations.

3. Analytical Methods

The characterization of S-C fabrics was performed by using optical and scanning electron microscopes at the Institute of Petrology and Structural Geology, Charles University in Prague. The geometry of S-C fabrics and quantitative microstructural analysis has been evaluated from digitized micrographs by using the polyLX MATLAB[TM] toolbox [*Lexa*, 2003].

The cathodoluminiscence analysis was performed using the TESCAN Vega scanning electron microscope (SEM) at the Charles University in Prague and hot cathodoluminiscence at optical microscope Olympus TH3 with HC2-LM system at the Masaryk University in Brno. Semiquantitative mineral chemistry analyses were initially carried out via energy-dispersive spectroscopy (EDS) analyses using an Oxford X-Max 50 EDS detector attached to the TESCAN SEM as described in, for instance, *Broussolle et al.* [2015] and *Jiang et al.* [2015]. These analyses were then complemented with quantitative analyses in selected samples using a microprobe JEOL JXA 8200 Superprobe with EDS and wavelength dispersive spectroscopy operating at Department of Earth Sciences,
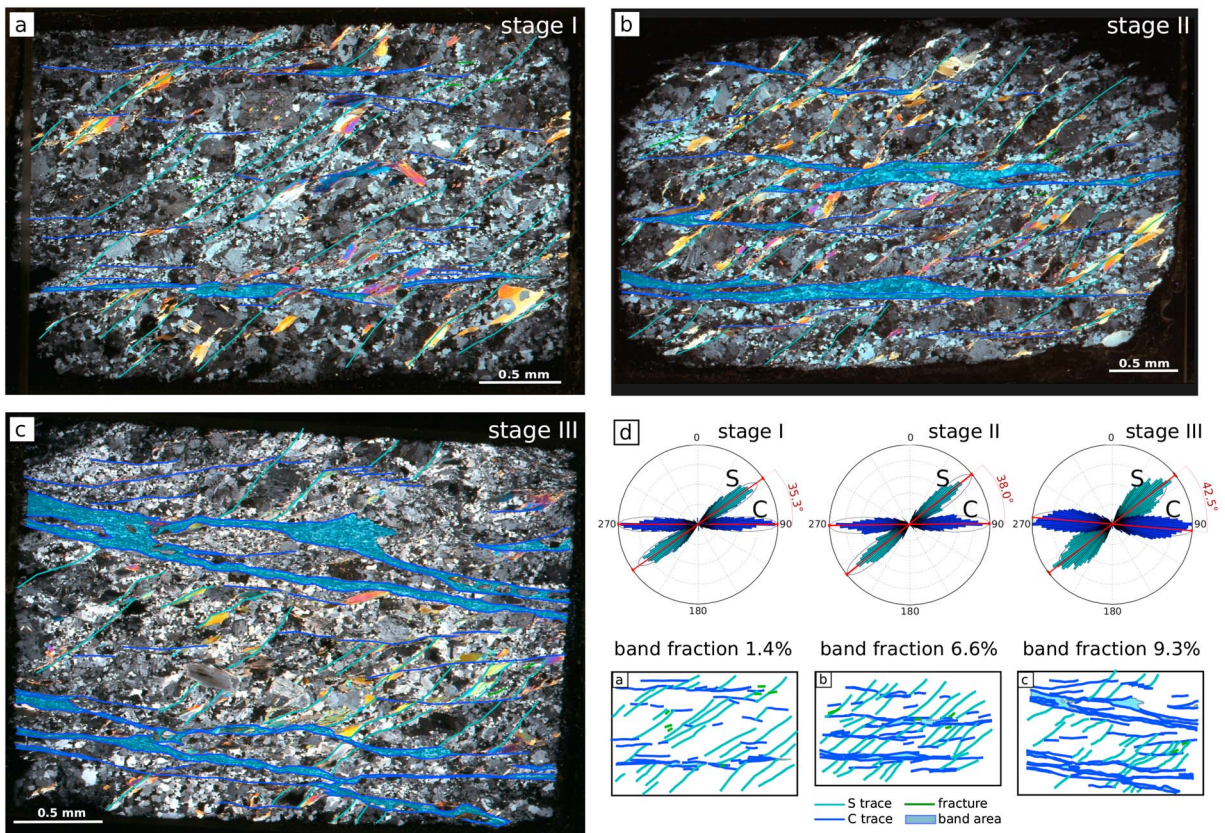
Figure 3. Thin section scans of three samples (series SB4) show typical evolutionary stages of shear band overprint from lowest in sample SB4B ((a) stage I), intermediate in sample SB4D ((b) stage II), to highest in sample SB4H ((c) stage III). Traces of S-C fabrics are marked in light blue (S) and dark blue (C), and the area occupied by the shear band matrix is highlighted by transparent blue. Microcracks are marked in green. (d) The length-weighted rose diagrams of segmented traces of S and C fabrics demonstrate orientation relationship between the two fabrics for the three stages (Figures 3a–3c). Mean-preferred orientation of S and C is indicated by the thick red line, and the standard deviation of orientation 1σ is shown by the red sections along the periphery of diagrams. The angle between mean orientation of S and C fabrics increases toward stage III, and the orientation of both fabrics becomes more scattered. The small thin section insets in Figure 3d demonstrate the increasing proportion of shear band matrix from stage I to stage III in (Figures 3a–3c).

Free University in Berlin. Chemical data were plotted using the Geochemical Data Toolkit [*Janoušek et al.*, 2006]. The effective bulk rock chemical analysis of shear bands used for thermodynamic modeling was obtained directly from thin sections by area scanning electron microscopy using the TESCAN Vega at the Institute of Petrology and Structural Geology in Prague.

Electron backscattered diffraction (EBSD) analysis was carried out using the field emission gun FEI Quanta[TM] 3-D FEG dual beam machine with an EDAX/TSL EBSD camera and orientation imaging microscopy (OIM) software operating at the GFZ Potsdam. The thin sections were first polished with diamond paste up to a 0.25 μm and then treated with chemical polish using the standard alkaline solution of colloidal silica of 0.015 μm for 4 h. The operating conditions of the SEM/EBSD were the following: accelerating voltage of 20 kV, beam current of 8 nm, and sample tilt of 70°. In individual EBSD scans, the working distance varied between 12 and 15 mm, and the step size varied between 5 and 20 μm. The EBSD data were plotted using the MTEX toolbox in MATLAB[TM] [*Hielscher and Schaeben*, 2008]. The transmission electron microscopy (TEM) was performed for three thin foils (0.15 μm thick) cut across phase boundaries of quartz-K-feldspar by using the FEI Tecnai G2 F20 X-Twin TEM at GFZ Potsdam. For details related to TEM foil preparation see *Wirth* [2009].

4. Characterization of S-C Fabrics

The studied thin sections revealed that the fabrics are characterized by distinct microstructures and minerals, which in case of K-feldspar and white mica show two generations. The S fabric is defined by shape-preferred orientation of relatively coarse-grained recrystallized quartz aggregates (Figure 2b) and larger grains of

K-feldspar I, plagioclase, and white mica I (approximately 0.5–4 mm in size). In contrast, the C fabric shear bands are represented by zones of fine-grained matrix comprising mixed K-feldspar II, quartz, and white mica II grains and in some samples also chlorite (Figures 2c and 2d). The studied samples were sorted into series on the basis of increasing intensity of shear band overprint manifested by increasing proportion of C fabric-related matrix at the expense of S fabric-related porphyroclasts and aggregates (Figure 3). Although it is difficult to directly link the intensity of overprint with strain due to the lack of clear displacement markers, the increasing proportion of C fabric matrix most likely reflects the evolution of shear bands. Indeed, the thin and isolated shear bands which likely correspond to the initiation stages are crosscut by wider and intercon- nected shear bands pointing to the maturation of shear bands with increasing proportion of the C fabric matrix (Figures 3b and 3c). The series SB4 from the Lescastel quarry (Figure 1) exemplify the typical increase in proportion of C fabric matrix which we identified as evolutionary stages (I–III) (Figure 3d). Stages I and III in most series are characterized by the proportion of C fabric matrix below and above 1.5% and 8%, respectively, and stage II has the matrix proportion in between the two values. The mineral assemblage of the C fabric matrix is identical for all stages.

In general, the samples characterized by low shear band overprint show short and discrete/thin shear bands while with increasing degree of overprint, shear bands become longer, wider, and interconnected. The angle between mean orientation of C and S fabrics in most series shows a gradual increase from ~35° for stage I up to ~42° for stage III C′ geometry (see rose diagrams in Figure 3d). This observation contrasts with the commonly observed decrease in the S-C angle with increasing intensity of deformation [e.g., *Berthé et al.*, 1979a]. However, this change is likely associated with the transition from C-type shear bands to C′-type shear bands toward the stage III as manifested by deformation in the relay ramp domains connecting individual segments of C bands (see abc sketches in Figure 3d). As a result of this transition, samples with higher intensity of shear band overprint show greater scatter in orientation of both C and S fabrics (Figure 3c). It is important to note that with the increasing shear band overprint in stage III when the proportion of C fabric matrix reaches 13%, the angle between S and C/C′ starts to decrease, and both fabrics become parallel/indistinguishable in the ultramylonite samples.

4.1. Microcracks and Shear Bands

Independent of the degree of shear band overprint, all studied samples contain cracks which crosscut the S fabric and show systematic orientations close to the orientation of shear bands (Figure 4). The microcracks can be clearly distinguished when crosscutting the recrystallized quartz aggregates and are best preserved in samples with lower intensity of shear band overprint, i.e., in stage I samples. The microcracks typically occur in the vicinity of large white mica I and plagioclase grains, enclosed within quartz aggregates, where they crosscut quartz grains or follow the existing grain boundaries (Figure 4a). The orientation of microcracks was traced in the thin section plane from five samples covering the three evolutionary stages. The orientation of traces of microcracks was characterized with respect to the reference line represented by the S fabric trace, and it is shown for all five samples in the cumulative histogram in Figure 4b. Here the angles between micro- cracks and S fabric are plotted using the probability density function. The resulting histogram shows polymo- dal orientation distribution with majority of the microcracks occurring close to the orientation of shear bands, i.e., at angles between 25° and 45° from the S fabric (Figure 4b). Other preferred orientations of microcracks are represented by the peak located in between the S and C fabric orientations at 12–25° from S and by two subordinate peaks close to S orientation at angles between 5° and 15° from S (Figure 4b). Microcracks at high angle to the S fabric are extremely rare. The microcracks are frequently filled with minerals typical for the assemblage observed in the studied shear bands. On the other hand, not all the microcracks are filled, and there seem to be a systematic relationship between orientation of microcracks and presence/absence of infill. Fifty-five percent of microcracks oriented close to the S fabric have the mineral infill with mainly white mica II and sometimes chlorite. Microcracks oriented at 12–25° to S show higher proportion of filled microcracks reaching 76%, which further increases to 90% for microcracks close to the shear band orientation (Figure 4b). These latter microcracks are filled by typical shear band assemblage represented by K-feldspar II, white mica II, and chlorite. The microcracks oriented at high angles to the S fabric lack the mineral infill completely. From these observations it is clear that the microcracks have some relationship to shear bands and that they most likely represent their thin precursors. The inflection of coarse-grained quartz microstructure in the recrystallized aggregates was further documented by the cold cathodoluminiscence revealing damage of quartz in the vicinity of the microcracks (Figure 4c).
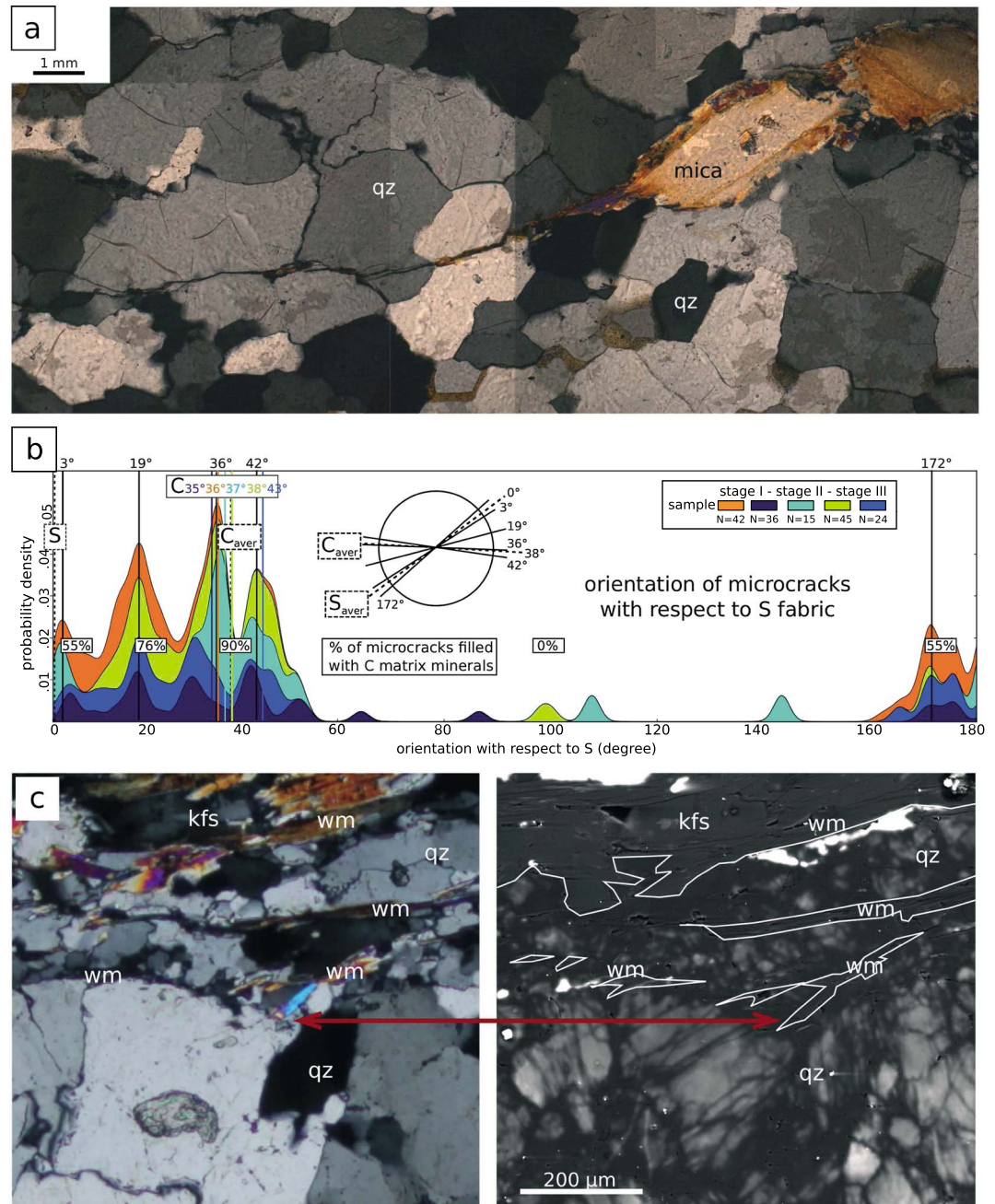
Figure 4. (a) Microphotograph of microcrack crosscutting recrystallized quartz aggregate. The microcrack is created at the tip of white mica porphyroclast. (b) Probability density function of microcrack orientation with respect to the S fabric. The orientation of microcracks was determined in five samples covering all stages of shear band evolution (stage I–III). Individual colors in the diagram correspond to individual samples (SB2A, SB4B, SB4D1, SB4F, and SB4H), and N indicates number of measured microcracks in each sample. The S fabric corresponds to 0° orientation, while C fabric orientation is indicated by colored lines for individual samples and black dotted line for average orientation. Summary diagram highlighting the peaks in orientation density of microcracks with respect to the average orientation of S and C fabrics is shown in the circular diagram. (c) Optical micrograph and the corresponding cathodoluminescence image show the disruption of quartz aggregate microstructure in the vicinity of a shear band (sample SB4D). The lighter parts of quartz grains correspond to original microstructure, while the darker parts indicate disruption of quartz grains associated with shear bands.

Table 1. Representative Mineral Chemistry Analyses of K-Feldspar, Plagioclase, White Mica, and Chlorite Obtained With Microprobe and SEM

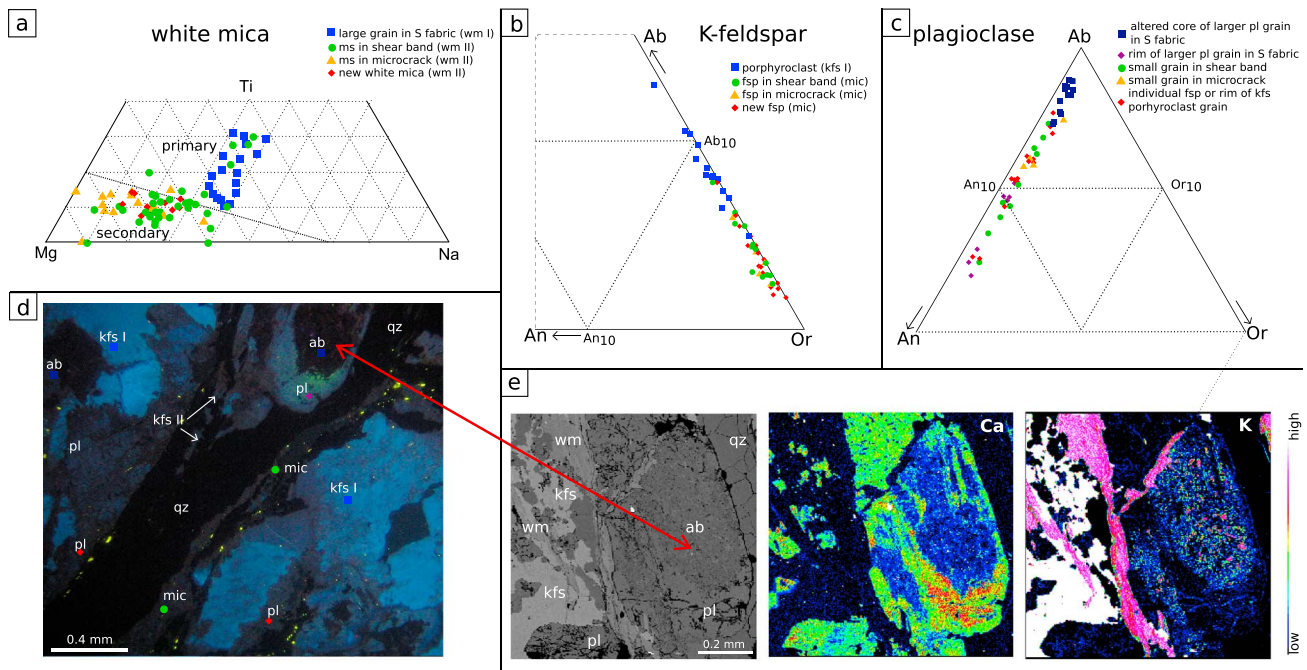| Mineral	K-Feldspar				Plagioclase			White Mica			Chlorite
Generation	Porphyroclast	Grain in Microcrack	Grain in Shear Band	Newly Grown Grain	Larger Grain Rim	Grain in Shear Band	Larger Grain Altered Core	Large Grain Core	Grain in Microcrack	Grain in Shear Band	Chlorite
	kfs I	kfs II (Microcline)	kfs II (Microcline)	kfs II (Microcline)	Plagioclase	Plagioclase	Albite	White Mica I	White Mica II	White Mica II	Chlorite
SiO_2	64.26	64.66	64.11	63.95	64.61	64.61	67.28	45.87	49.73	46.32	37.48
TiO_2	0.04	0.00	0.02	0.00	0.00	0.00	0.00	0.60	0.00	0.34	1.33
Cr_2O_3	0.01	0.01	0.03	0.01	0.00	0.00	0.04	0.01	0.00	0.02	0.00
Al_2O_3	18.51	18.53	18.02	18.13	21.75	21.75	19.93	34.21	34.57	33.30	21.80
FeO	0.02	0.00	0.02	0.00	0.01	0.01	0.00	1.82	0.50	2.38	19.70
MnO	0.03	0.00	0.04	0.03	0.01	0.01	0.01	0.04	0.00	0.05	0.43
MgO	0.00	0.00	0.02	0.00	0.00	0.00	0.00	0.67	0.82	1.00	1.99
CaO	0.04	0.09	0.03	0.03	2.80	2.80	0.52	0.01	0.00	0.01	0.21
Na_2O	0.89	0.46	0.32	0.24	9.63	9.63	11.13	0.44	0.07	0.33	0.08
K_2O	15.45	16.22	16.24	16.46	0.21	0.21	0.07	10.77	9.95	10.96	5.53
sum	99.25	99.97	98.84	98.84	99.03	99.03	98.99	94.44	95.65	94.71	88.55
Si	2.98	2.99	3.00	3.00	2.87	2.88	2.98	3.09	3.32	3.12	4.10
Ti	0.00	0.00	0.00	0.00	0.00	0.00	0.00	0.03	0.00	0.02	0.11
Cr	0.00	0.00	0.00	0.00	0.00	0.00	0.00	0.00	0.00	0.00	0.00
Al	1.01	1.01	0.99	1.00	1.14	1.14	1.04	2.72	2.72	2.64	2.81
Fe^{3+}	0.00	0.00	0.00	0.00	0.00	0.00	0.00	0.02	0.00	0.07	0.00
Fe^{2+}	0.00	0.00	0.00	0.00	0.01	0.00	0.00	0.08	0.03	0.06	1.80
Mn	0.00	0.00	0.00	0.00	0.00	0.00	0.00	0.00	0.00	0.00	0.04
Mg	0.00	0.00	0.00	0.00	0.00	0.00	0.00	0.07	0.08	0.10	0.32
Ca	0.00	0.00	0.00	0.00	0.13	0.13	0.02	0.00	0.00	0.00	0.02
Na	0.08	0.04	0.03	0.02	0.83	0.83	0.95	0.06	0.01	0.04	0.02
K	0.92	0.96	0.97	0.98	0.02	0.01	0.00	0.93	0.85	0.94	0.77
sum	5.00	5.00	5.00	5.00	5.00	5.00	5.00	7.00	7.00	7.00	10.00
X Mg								0.40	0.74	0.43	0.15

Figure 5. Chemical composition of white mica and feldspars. (a) Mg-Ti-Na ternary diagram shows compositions of white mica grains from different samples and from distinct locations with respect to the C fabric (for color coding see legend and example in Figure 5d). (b) Anorthite-Albite-Orthoclase ternary diagram shows composition of K-feldspar grains (for color coding see legend and example in Figure 5d). (c) Anorthite-Albite-Orthoclase ternary diagram shows composition of plagioclase grains (for color coding see legend and example in Figure 5d). (d) Cathodoluminiscence image of a selected region in the vicinity of a shear band (sample SB7C) demonstrates distinct cathodoluminiscence for different generations of feldspar grains. For symbols and color coding of different feldspars see legend in Figures 5b and 5c). (e) BSE image and corresponding calcium and potassium element maps from the vicinity of a shear band. Mineral abbreviations used in the figure are as follows: kfs: K-feldspar, mic: microcline, pl: plagioclase, qz: quartz, and wm: white mica.

4.2. Mineral Chemistry of S and C Fabrics

The studied orthogneiss is composed of quartz, K-feldspar, plagioclase, white mica, apatite, zircon, sometimes also chlorite, and accessory tourmaline, monazite, rutile enclosed within biotite, hematite, and ilmenite (further description of these rocks can be found in *Tartèse and Boulvais* [2010]). As the white mica, K-feldspar, and plagioclase represent dominant components of the rock as well as the S and C fabrics building elements, our chemical analysis focused on these phases to characterize chemical differences between the two fabrics.

White mica occurs in all studied samples and has been identified in both S and C fabrics. In the S fabric, the white mica I has a form of large grains up to 4 mm in size (Figure 2b). When affected by the shear bands, the white mica I porphyroclasts bends toward the orientation of C fabric and/or recrystallize into fine-grained white mica II (Figure 2d). Moreover, small grains of white mica II form also outside the shear bands. The composition of both varieties of white mica corresponds to muscovite although the white mica II is little more phengitic (Table 1). Chemical analyses revealed further compositional differences between the two white micas demonstrated by variation in magnesium, titanium, and sodium contents (Figure 5a). The white mica I has the highest content of titanium (up to 0.08 atoms per formula unit—a.p.f.u.) and sodium (up to 0.07 a.p.f.u.) while the white mica II is low in titanium (up to 0.02 a.p.f.u.) and sodium (up to 0.03 a.p.f.u.) and rich in magnesium (up to 0.17 a.p.f.u., Table 1 and Figure 5a). The observed differences follow the previously proposed distinction between primary (magmatic) and secondary (metamorphic) muscovites [*Miller et al.*, 1981; *Tartèse and Boulvais*, 2010]. The diagram in Figure 5a shows that some smaller white mica grains in the shear bands have comparable composition to white mica I porphyroclasts implying the presence of reworked porphyroclast relics inside the shear bands. In addition, the white mica II in microcracks is a little higher in magnesium (up to 0.23 a.p.f.u.) and more phengitic (Si up to 3.33 a.p.f.u.) compared to white mica II in the well-developed shear bands (Si up to 3.13 a.p.f.u., Table 1).

K-feldspar occurs in two varieties represented by larger grains (K-feldspar (kfs) I) with their shape-preferred orientation parallel to S fabric and smaller irregular grains (kfs II) within shear bands (Figure 5). The K-feldspar
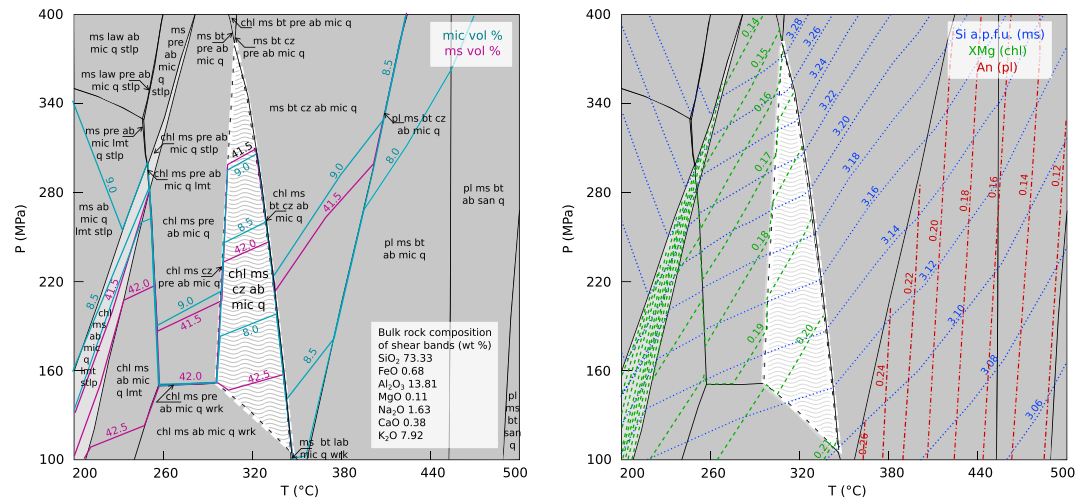
Figure 6. P-T section calculated for bulk shear band composition in sample SB4H by using thermodynamic software Perplex version 6.6.8 [*Connolly*, 2005] in the MnNCKFMASH system with water in excess. The modal isopleths of microcline and white mica content (in vol %) are shown in the image to the left. The compositional isopleths of XMg in chlorite, Si in white mica and anorthite component in plagioclase are shown in the image to the right. The stability field of observed shear band assemblage is highlighted by dashed white line, and its range corresponds to the resulting P-T estimate.

composition is similar to the binary solution with orthoclase component in the range of 86.7–99.6%, albite component between 1.7 and 12.9%, and negligible anorthite component between 0 and 0.9% (Figure 5b and Table 1). The large K-feldspar I grains are characterized by higher albite content between 7 and 13% while in the K-feldspar II albite component is lower (Figure 5b). The K-feldspar I is frequently replaced/encircled by irregular rims of plagioclase (Figure 5c). In some samples these plagioclase rims are mixed with quartz (myrmekites) and form parallel to the S fabric. The transmission electron microscopy revealed that the K-feldspar II in microcracks and shear bands is represented by microcline.

Plagioclase is represented by larger grains with their shape-preferred orientation parallel to S fabric (Figures 2 and 3) and by smaller grains within the S fabric as well as within shear bands. The composition of plagioclase ranges from oligoclase to albite with 80.0–97.7% of albite component, 1.7–19.5% anorthite component, and minor orthoclase component between 0.4 and 1.9% (Figure 5c and Table 1). The larger plagioclase grains show systematic zoning pattern with albite rich cores and more anorthite rich rims (Figures 5d and 5e). The cores, however, are formed by a mixture of albite and small white mica II grains (Figure 5e). The rims have the composition of oligoclase which is common also for smaller plagioclase grains in the S fabric and plagioclase rims around K-feldspar I porphyroclast (Figures 5c–5e). Small plagioclase grains that are locally present within shear bands have similar compositional range as the above mentioned S-related plagioclase (Figure 5c) and thus could represent relict grains that were reworked by shear bands. On the other hand, some of the smaller plagioclase grains in microcracks show more albite rich composition (Figure 5c) suggesting that albite forms synchronously with shear bands as a stable part of the C fabric-related assemblage.

Chlorite is present in a form of individual grains, which are found in microcracks and in the shear bands and their vicinity. The chlorite grains are small, typically up to 0.5 mm, and their XMg content reaches 0.15–0.21 (Table 1).

4.3. P-T Conditions of Shear Band Formation

Phase equilibrium approach was used to characterize pressure-temperature (P-T) conditions of shear band formation at locality SB4 in the Questembert granite (Figure 1). The bulk chemical composition of the studied shear bands was estimated by using the scanning mode of the electron microscope. The shear band mineral assemblage common to all stages was scanned and averaged from the well-developed stage II and III shear bands in order to produce the effective bulk rock composition related to formation of shear bands (Figure 6). The P-T section and compositional isopleths were calculated using the Perple_X thermodynamic software [*Connolly*, 2005], version 6.6.8, with the internally consistent thermodynamic data set of *Holland and Powell* [1998: version 2004]. The preferred system for calculation was Na_2O–CaO–K_2O–FeO-MgO-Al_2O_3-SiO_2-H_2O (NCKFMASH) with water in excess. The resulting P-T section has been calculated with following solution models:
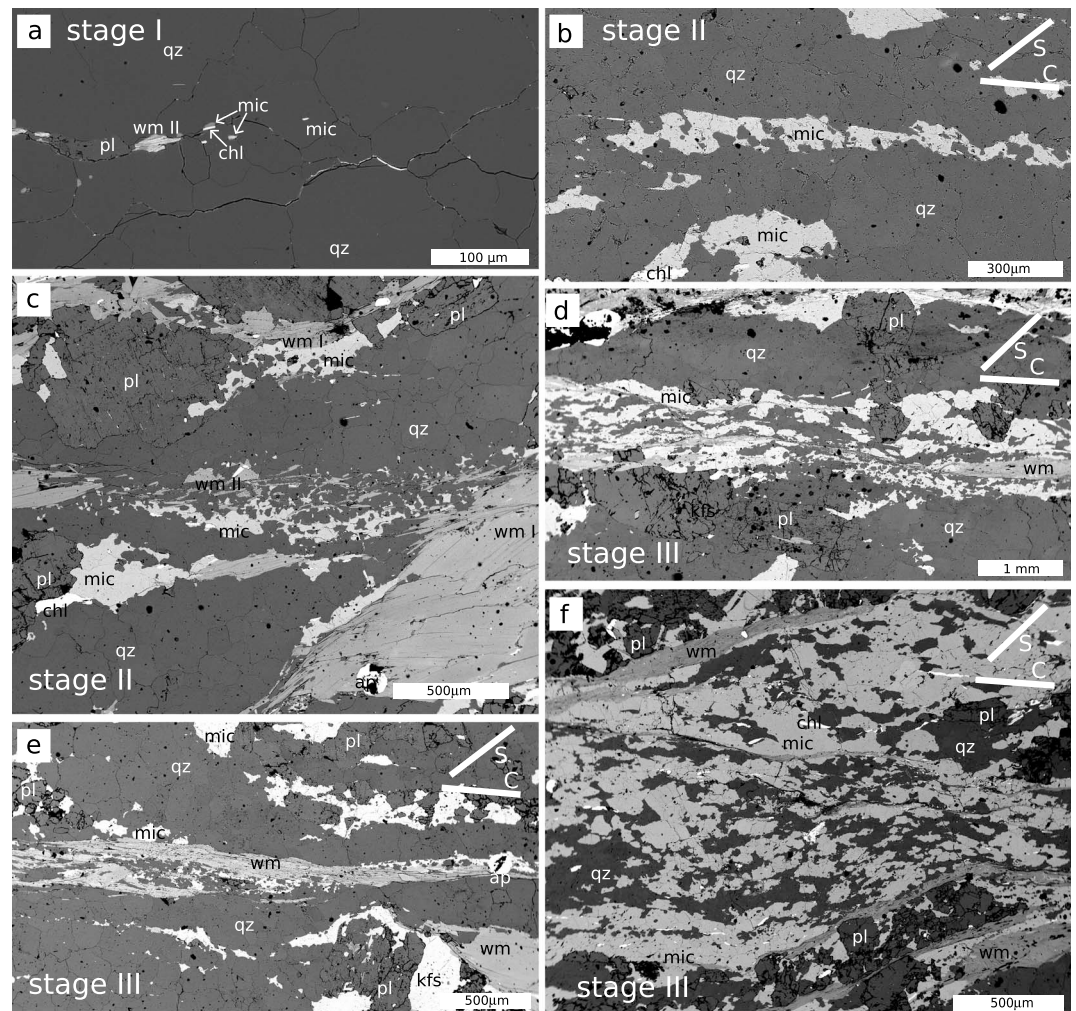
Figure 7. BSE images showing characteristic microstructures for individual stages I–III of shear band development. The particular stages of shear band evolution and general orientation of C and S fabrics are indicated in each image. (a) Microcrack crosscutting the quartz aggregate in stage I is filled with phengitic white mica II, microcline, plagioclase and chlorite (sample SB2A). (b) Microcline replaces quartz along shear bands in stage II (sample SB4D). (c) Quartz aggregate, plagioclase and white mica I porphyroclasts from the S fabric are reworked/replaced by shear band matrix composed of quartz white mica II and microcline in stage II (sample SB4D). (d–f) White mica grains form interconnected bands crosscutting the earlier shear band microstructure composed of microcline-quartz in stage III (Figures 7d and 7f—sample SB4H, Figure 7e—sample SB4D). The white mica bands overprint thin (Figure 7e) as well as thick (Figure 7f) shear bands. Mineral abbreviations used in the figure are as follows: ap: apatite, chl: chlorite, mic: microcline, pl: plagioclase, qz: quartz, wm I, wm II: white mica of first and second generation.

Ti-Fe-Mg-Mn biotite (extended from *Powell and Holland* [1999]), chlorite (extended from *Holland et al.* [1998]), white mica [*Coggon and Holland*, 2002; *Auzanneau et al.*, 2010], plagioclase [*Newton et al.*, 1980], and garnet [*Holland and Powell*, 1998].

In the resulting P-T section (Figure 6), the observed shear band assemblage of white mica II, chlorite, albite, and microcline best matches the stability field of white mica, chlorite, albite, microcline, and clinozoisite. In the lower temperature parts of the P-T section, the Ca-bearing phase is represented by clinozoisite, which appears when oligoclase is replaced by albite (Figure 6). Although clinozoisite was not observed in the studied rocks, it substitutes for another Ca-bearing phase represented by scarce apatite, which is not included in the thermodynamic data set and thus cannot be used in the P-T section. As the two phases are dominated by Ca, they do not exchange elements with other members of the shear band assemblage, and therefore, this substitution will not influence the resulting P-T estimate. For this reason the modeled assemblage of white mica-chlorite-albite-microcline-clinozoisite is considered as corresponding to the observed
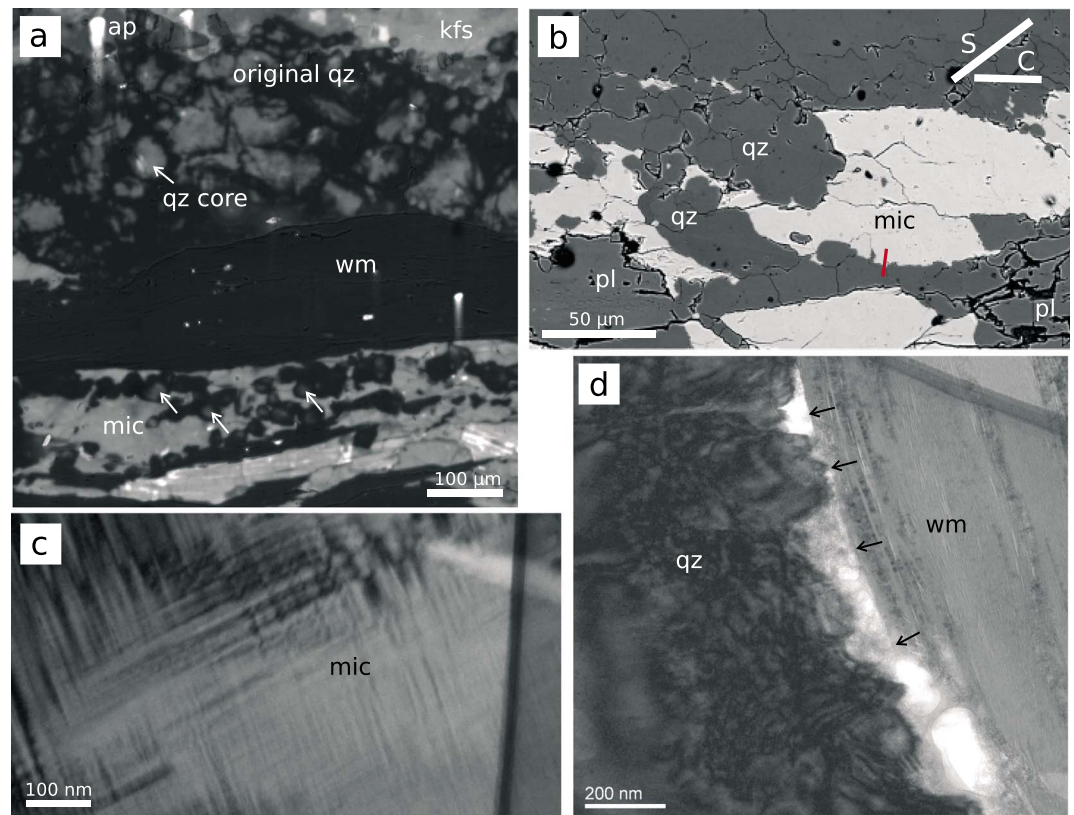
Figure 8. (a) Cathodoluminiscence image from the boundary between shear band (lower part) and quartz aggregate (upper part) in sample SB4H. The upper part of the image shows disintegration of the quartz aggregate microstructure, while the lower part of the image shows individual quartz grains enclosed by microcline inside the shear band. Cores of these individual grains (white arrows) exhibit identical luminescence as the original quartz grains in aggregates. (b) BSE image of microcline-quartz microstructure in stage II showing locations of TEM foil (red line). (c) The microcline twinning associated with transition of higher temperature magmatic K-feldspar to microcline is locally observed in relict grains surrounded by microcline without twinning in stage II shear bands. (d) The interface of white mica and quartz, where white mica precipitation causes dissolution of quartz and formation of porosity (white filled with epoxy in the sample).

assemblage within shear bands. The stability of the white mica-chlorite-albite-microcline-clinozoisite field is limited by disappearance of chlorite toward higher temperatures and by appearance of prehnite toward lower temperatures. The compositional range for chlorite and white mica II in the studied rocks fits well with the assumed stability field. However, because XMg in chlorite ranges between 0.15 and 0.21 and Si content in white mica II ranges between 3.08 and 3.29 a.p.f.u., the compositional isopleths cover full range of the assumed stability field, and further restriction of P-T estimate was not possible. Thus, the resulting P-T conditions for shear band assemblage correspond to the extent of the white mica-chlorite-albite-microcline-clinozoisite stability field, i.e., to 300–350°C and 100–400 MPa (Figure 6). The plagioclase associated with the S fabric shows compositional range between 6 and 16% of anorthite component, which in the calculated P-T section corresponds to temperatures higher than 445°C (Figure 6). This rough temperature estimate for the S fabric formation is in a good agreement with the relatively high temperature (~500–550°C) [cf. *Stipp et al.*, 2002; *Jeřábek et al.*, 2007], quartz deformation microstructure in the recrystallized aggregates related to S fabric (Figures 2b and 2c).

4.4. Microstructure of Shear Bands

In the following text we describe microstructural relationships in the shear bands for each of the evolutionary stages I–III, documented from samples with increasing intensity of shear band overprint. The thin and separated bands in samples with low intensity of shear band overprint are characteristic for stage I, better represented by microstructure of filled microcracks (Figure 7a). The stages II and III are associated with well-developed shear bands characterized by microstructure in thicker and more interconnected bands (Figures 7b–7f).
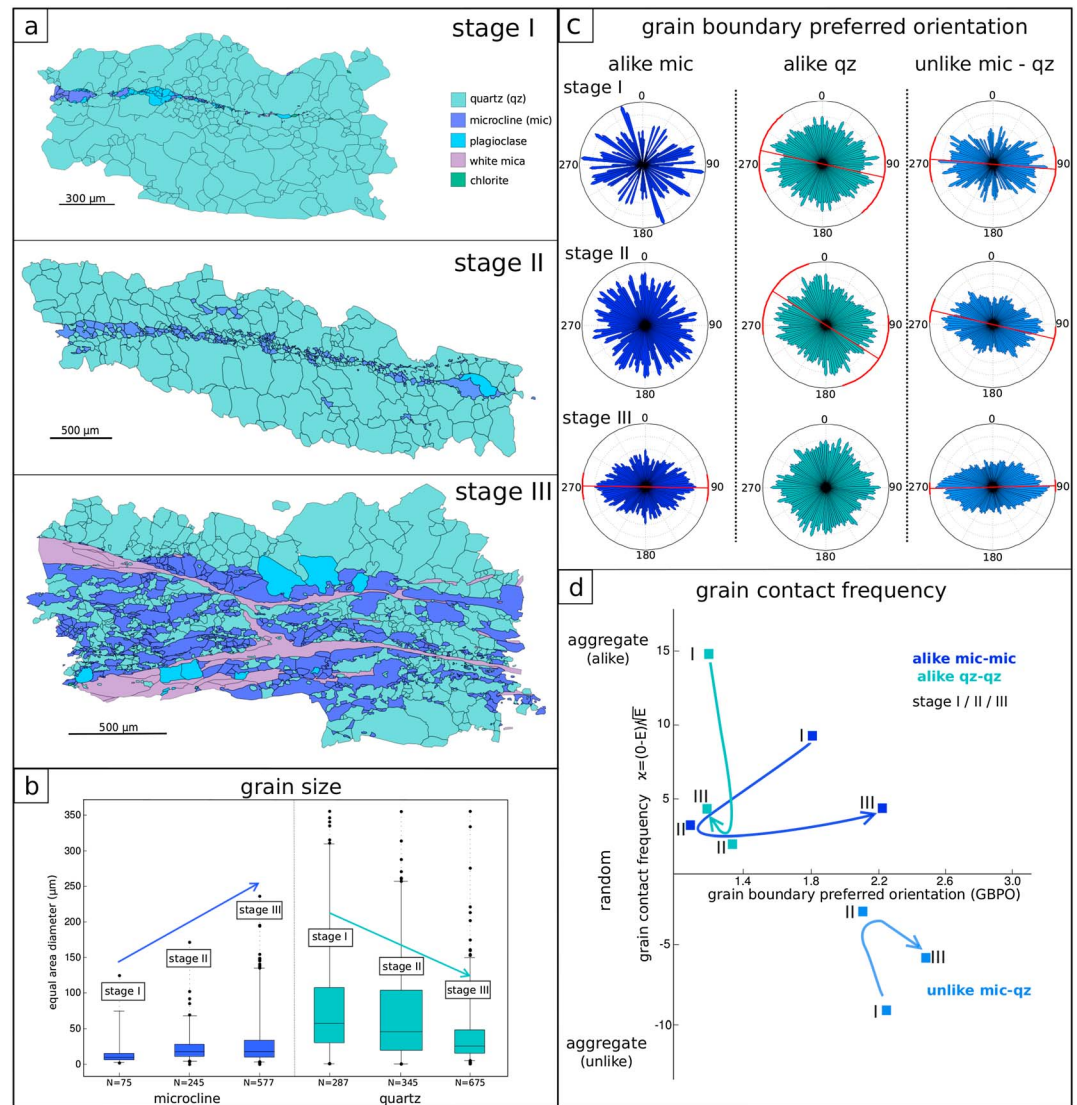
Figure 9. Results of quantitative microstructural analysis from digitized microstructures related to (a) stage I (sample SB2A), stage II (sample SB4D), and stage III (sample SB4H) of shear band evolution. (b) The box plots for microcline and quartz grain size from individual stages I–III demonstrate an increase in size of microcline grains and decrease of quartz grains from stage I to III including all the grains in the depicted microstructure (also the grains from original S fabric). N indicates the number of analyzed grains. (c) Weighted rose diagrams show grain boundary-preferred orientation obtained from the digitized grain maps of microcline alike (like-like) boundaries, quartz alike boundaries and microcline-quartz unlike boundaries for individual stages I–III. The red line in diagrams shows mean orientation and the red sections along the periphery of the diagrams show the orientation within standard deviation (1σ). (d) The results of grain contact frequency analysis [*Kretz*, 1969] of alike and unlike boundaries for microcline and quartz for individual stages I–III plotted against grain boundary-preferred orientation. All analyzed contacts show similar evolution trends, i.e., from aggregate distribution in stage I via randomization characteristic for stage II to more aggregate distribution toward stage III.

The filled microcracks of stage I show individual small grains of albitic plagioclase, microcline, white mica II, and/or chlorite decorating microcrack surfaces (Figure 7a). Stage II shows shear band widening associated with formation of microcline, and the bands are dominated by fine-grained mixture of microcline and quartz (Figures 7b and 7c). The contact of the two phases is characterized by typical curved shaped or bulged grain boundaries suggesting that microcline is invading quartz (Figure 8b). The TEM analysis of the quartz-microcline boundaries shows dissolution of quartz and growth of microcline. This observation is further supported by the cathodoluminescence images showing small relict quartz grains surrounded by the newly formed microcline, with their cores having identical luminescence as the neighboring large quartz grains
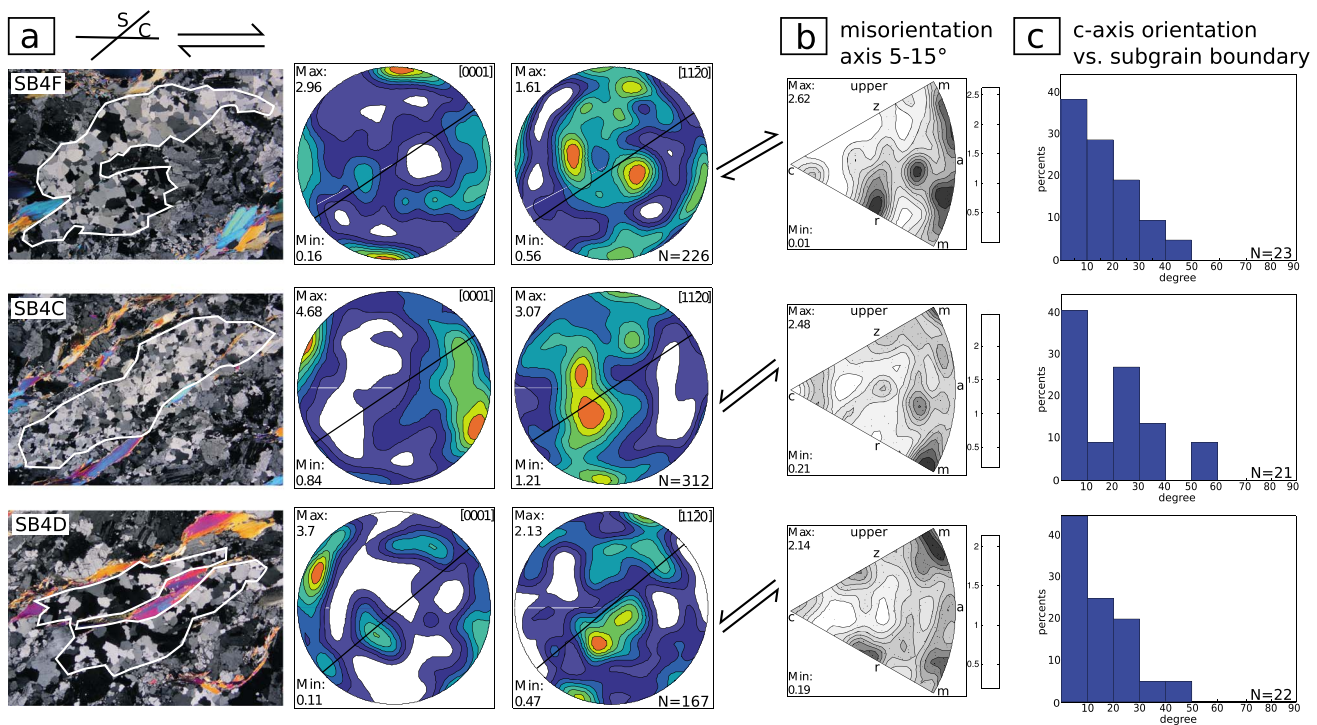
Figure 10. Results of crystal-preferred orientation (CPO) analysis of quartz aggregates defining the S fabric. (a) Microphotographs of quartz aggregates used for EBSD mapping and corresponding pole figures of quartz CPOs (samples SB4C, SB4F, and SB4D). The orientation of C and S fabrics is indicated in the microphotographs, and orientation of S fabric is indicated by solid black line in each pole figure. The overall kinematic frame can be compared with the shear sense determined from the S fabric aggregates for each sample by using the criterion of inclination of CPO with respect to orientation of the S fabric. (b) Inverse pole figures show position of misorientation axes with respect to the crystal reference frame for the 5–15° misorientation interval. (c) The histograms showing angular relationship between C axis of subgrains and trace of subgrain boundaries determined by U-stage from quartz aggregates defining the S fabric in corresponding samples in Figure 10a. The histograms show prevailing low angle relationships suggesting operation of basal $<a>$ slip system.

in the recrystallized aggregates (white arrows in Figure 8a). Thus, the original quartz microstructure of S fabric aggregates seems to be disintegrated by invading microcline which replace quartz along shear bands and quartz grain boundaries (Figures 7b, 7c, and 8b). Toward the stage III, white mica II starts to be frequent in the C fabric matrix (Figures 7c and 7d). The microstructure associated with stage III is characterized by bands of interconnected white mica that in a number of cases intersects and offsets quartz and microcline grains (Figures 7d and 7e). The increasing proportion of white mica and the progressive interconnection in the direction parallel to shear bands lead to the separation of domains, where mixtures of quartz and microcline represent the inactive relict microstructure related to stage II deformation. In the micaceous bands the white mica II shows features characteristic for dissolution of quartz and K-feldspar (Figure 8d). The progress of shear band widening and interconnection (Figure 7f) may eventually lead to formation of ultramylonites characterized by significant decrease in grain size and complete phase mixture.

4.5. Quantitative Microstructural Analysis of Shear Bands

The microstructures of mixed quartz and microcline related to the three stages of shear band evolution (Figure 9a) have been evaluated from digitized backscattered electron (BSE) and optical micrographs at localities SB2 and SB4 (Figure 1) by comparing grain parameters such as size, shape-preferred orientation, and contact frequency. The grain diameter is specified as diameter of a circle with the grain equivalent area, and it was determined for both quartz and microcline (Figure 9b). The median grain size (and interquartile range IQR) of microcline steadily increases from 7 μm (IQR = 5–12 μm) for stage I, to 18 μm (IQR = 12–28 μm) for stage II, and 17 μm (IQR = 8–25 μm) in stage III (Figure 8b). In contrast, the median grain size of quartz decreases from 46 μm (IQR = 23–85 μm) for stage I, to 45 μm (IQR = 19–103 μm) for stage II, and to 19 μm (IQR = 11–23 μm) for stage III. The presented quartz grain-size analysis covers both S and C fabric microstructures and as such aims to demonstrate the continual dismembering of the S fabric aggregates. The length-weighted orientations of grain boundaries presented in rose diagrams (Figure 9c) have been evaluated separately for alike and unlike
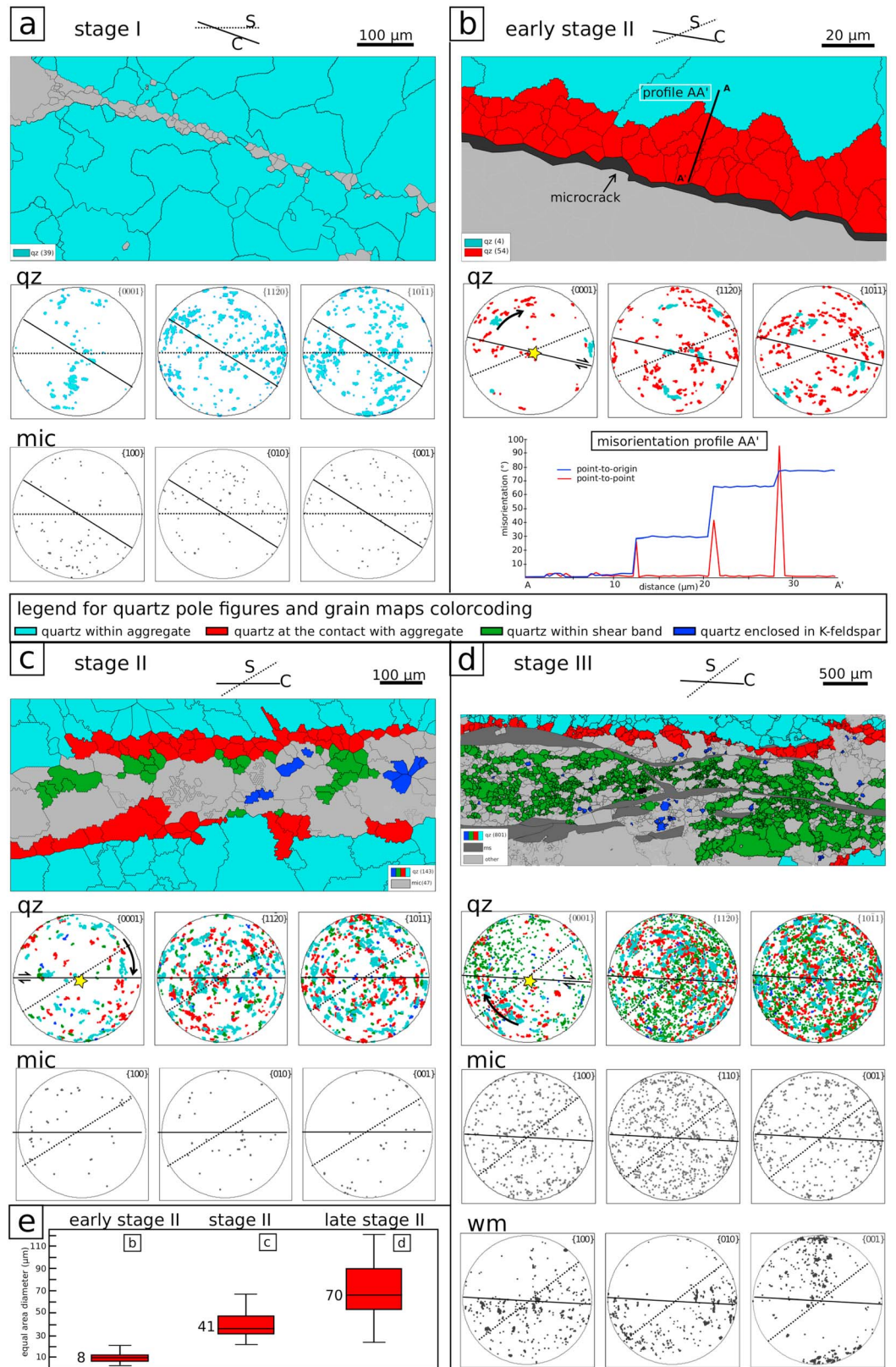
Figure 11

phase contacts, i.e., for quartz-quartz, microcline-microcline, and quartz-microcline contacts (Figure 9c). From stage I to stage III, the rose diagrams clearly demonstrate the change in shape of microcline grains from equiaxed to elongated, with long axes parallel to shear bands while quartz grains generally maintain the equiaxed shape. The quartz-microcline phase contacts in all three stages show preferred orientation parallel to shear bands (Figure 9c). The grain contact frequency for alike and unlike phase contacts was evaluated using the grain contact frequency method of *Kretz* [1969, 1994]. In his method, the grain contact frequency number (χ) expresses a deviation from random distribution of phases. For alike phase contacts χ is positive for aggregate, zero for random, and negative for regular distributions, and this relationship is reversed for unlike phase contacts. The results of grain contact frequency analysis of quartz-quartz, microcline-microcline, and quartz-microcline contacts show identical trends in evolution from stage I to stage III (Figure 9d). The transition from stage I to stage II indicates randomization of the inherited aggregate distribution of phases (Figure 9d). In contrast, the transition from stage II to stage III show reversed trend and the evolution from more random toward more aggregate distribution of quartz and feldspar. At the same time the grain boundary-preferred orientation of microcline becomes stronger while the one of quartz weakens. The intersecting crystallization relationships of white mica II with respect to quartz and microcline in the late period of stage III suggests that the growth of mica postdated the above described mixing/unmixing of quartz and microcline phases.

4.6. Crystallographic-Preferred Orientation of Selected Minerals From S-C Fabrics

The crystallographic-preferred orientation of quartz from recrystallized aggregates in the S fabric and of quartz, microcline, and white mica from shear bands has been characterized by means of electron backscattered diffraction (EBSD) method.

4.6.1. Crystallographic-Preferred Orientation of Quartz in S Fabric

Crystallographic orientation of quartz has been evaluated from recrystallized aggregates defining the S fabric. Due to the relatively coarse-grained microstructure of quartz aggregates (see Figure 9b), large portions of thin sections had to be analyzed to produce representative orientation data set covering at least 150 quartz grains. Furthermore, the overprinting effects related to shear bands in their proximity were avoided.

The crystallographic-preferred orientation (CPO) of quartz aggregates show single maxima and single girdle patterns (Figure 10a). In the [0001] *c* axis diagrams, the CPO maxima are located at the periphery of the pole figures at 60–70° angle from the S fabric (Figure 10a). These maxima suggest activity of basal ‹a› slip system. At the same time, weak single girdles of *c* axis occur close to the orientation of S fabric with maxima in the vicinity of its lineation suggesting activation of prism [c] slip (Figure 10a). Indeed, if the tilt boundaries are assumed, the axes of low angle misorientations plotted into the inverse pole figure (Figure 10b) suggest dominant basal ‹a› or prism [c] and some contribution of rhomb ‹a› slip systems. As the misorientation analysis cannot distinguish between basal ‹a› and prism [c] [*Lloyd*, 2004], the universal stage was applied to confirm or

Figure 11. Crystallographic-preferred orientation of main phases for individual stages I–III of shear band evolution. (a) Stage I (sample SB2A) shows quartz aggregate (light blue) crosscut by microcrack filled with microcline, white mica and chlorite (shown in grey). The corresponding pole figures show CPO of quartz aggregate related to formation of S fabric and CPO of microcline grains in the microcrack. (b) Stage I (sample SB4E) showing recrystallization of quartz aggregate along microcrack (black). The quartz grain map shows parent (light blue) and recrystallized (red) grains along the microcrack. Identical color-coding has been used in the pole figures. The recrystallized grains with respect to the parent grains show clockwise rotation around misorientation axis indicated by yellow star in the pole figure. The misorientation profile AA' marked in the grain map shows evolution in misorientation angle from parent grain toward fracture (blue line) as well as relative misorientation angle between individual grains (red line). (c) Stage II (sample SB4D) shows portions of recrystallized quartz grains encircled by microcline within the shear band (dark blue quartz, grey microcline), quartz grains within the shear band maintaining the contact with aggregate (green) and recrystallized quartz grains (red) along the contact between shear band and quartz aggregate (light blue). The corresponding CPO's of these distinct quartz grains are shown in pole figures using identical color-coding. The misorientation axis between parent and recrystallized grains is indicated by yellow star. The pole figures for microcline show weak CPO. (d) Stage III (sample SB4H, corresponds to Figure 9a and part of Figure 6d) shows grain maps and pole figures with identical color coding as in Figure 11c. The misorientation axis between parent (light blue) and recrystallized (red) quartz grains is again indicated by yellow star. The CPO of quartz grains (green and blue) encircled by microcline shows scattering of orientations away from the orientations of recrystallized grains (red) along the contact between shear band and quartz aggregate. K-feldspar in the shear band is characterized by random CPO, while white mica reveals strong CPO with basal planes being mostly parallel to the shear band. The pole figures represent projection on the upper hemisphere. (e) Grain size (equal area diameter) of recrystallized quartz grains along the contact with aggregate determined from Figures 11b–11d (only the red grains were used) show increase in size of dynamically recrystallized grains from early to late stage II (the mean size is indicated next to each boxplot).

disprove the two slip systems by measuring the angle between the orientation of subgrain boundaries and c-axes of subgrains [e.g., *Okudaira et al.*, 1995]. At least 20 pairs of subgrain boundary-subgrain c axis from each of the three samples at locality SB4 (Figure 1) were analyzed (Figure 10 c) indicating that the c-axes are mostly subparallel to subgrain boundaries. This confirmed the prevalence of the basal ‹a› slip and excluded the operation of prism [c] slip [cf. *Okudaira et al.*, 1995]. It is interesting to note that the single maxima related to basal ‹a› slip show both synthetic and antithetic rotations with respect to overall shear sense indicated by the S-C fabrics geometry (Figure 10a). The presence of weak subordinate c axis girdle in most analyzed samples remains unclear, as it may either correspond to weak contribution of prism [c] slip during the formation of S fabric or it may be related to the subsequent overprint associated with formation of shear bands.

4.6.2. Crystallographic-Preferred Orientation in Shear Bands

The CPO of quartz in the vicinity of shear bands documents modification/overprint of the aggregate CPO in the S fabric. In the early stages of shear band formation (stage I) associated with microcracking the overprint is insignificant and the aggregates still preserve the original CPO (aggregate grains in light blue; Figure 11a). This changes toward stage II when the microcracks become active slip surfaces and impose recrystallization of coarse-grained quartz microstructure in the vicinity of microcracks (recrystallized grains in red; Figure 11b). The misorientation angle profile AA′ in Figure 11b demonstrates that subgrains are formed in the large quartz grains related to the S fabric microstructure. Moreover, it also demonstrates a continuous rotation of small independent recrystallized grains away from the orientation of the parent grains. These observations point to the rotation recrystallization mechanism that is active during the slip along the shear bands. The misorientation axis between parent and recrystallized grains occurs in the shear band plane and is perpendicular to the shear band lineation (star in the center of pole figures in Figure 11) indicating the formation of tilt boundaries and activity of basal ‹a› slip system [e.g., *Neumann*, 2000]. In addition, the clockwise rotation of lattice of the recrystallized grains away from the orientation of aggregate grains (black arrows in Figure 11) is consistent with the dextral shearing along shear bands and thus documents the relationship between recrystallization and slip along the microcracks.

The stage II of shear band development is marked by the formation of microcline disintegrating the recrystallized quartz microstructure along shear bands. This process leads to separation/isolation of parts of recrystallized quartz microstructure being surrounded by the newly formed microcline (recrystallized grains attached to aggregates in green and recrystallized grains enclosed by microcline in dark blue; Figure 11c). At the same time, slip along shear bands and quartz recrystallization continued as documented (1) by the presence of recrystallized quartz grains along the contacts between aggregates and shear bands and (2) by randomization of quartz CPO shown by isolated quartz grains within shear bands (Figures 11c and 11d). The CPO of microcline is very weak to absent (Figures 11c and 11d). The grain size of recrystallized quartz grains along the contact between an aggregate and shear band (red grains in Figure 11) increases with increasing width of shear bands from stage I to stage III (Figure 11e). The stage III of shear band development is associated with formation of interconnected white mica bands. The white mica show strong CPO with their basal planes oriented subparallel to shear bands (Figure 11d).

5. Discussion

5.1. S-C Fabrics in the South Armorican Shear Zone: Their Origin and Geometry

The origin and mechanical importance of S-C fabrics has been discussed for decades since their first recognition in the South Armorican Shear Zone by *Berthé et al.* [1979a, 1979b]. Two principal scenarios explaining the formation of S and C fabrics as synchronous or diachronous are commonly assumed [e.g., *Lister and Snoke*, 1984]. The synchronous S-C/C′ fabrics are usually reported from major crustal shear zones where their evolution is associated with partitioning of deformation or variation in the intensity of shear strain [*Berthé et al.*, 1979a; *Platt*, 1984; *Blenkinsop and Treloar*, 1995; *Schulmann et al.*, 1996; *Fusseis and Handy*, 2008]. The diachronous S-C/C′ fabrics are explained either as sequential overprint of metamorphic foliation (S) by narrow shear bands (C/C′) formed during single kinematic event due to cooling and localization [e.g., *White et al.*, 1980; *Gapais and White*, 1982; *Knipe and Wintsch*, 1985; *Gapais*, 1989; *Gillam et al.*, 2014] or as cleavage overprinting an earlier and kinematically unrelated metamorphic foliation [e.g., *Platt and Vissers*, 1980; *Bukovská et al.*, 2013].

The studied S-C fabrics in the major right-lateral South Armorican Shear Zone develop in granitoid plutons that were emplaced synkinematically relative to SASZ between 338 and 329 Ma and affected by shearing

as late as 300 Ma [*Tartèse et al.*, 2011, 2012]. These S-C/C' fabrics were previously interpreted as synchronous [*Berthé et al.*, 1979a, 1979b] or diachronous and resulting from single kinematic event as a result of cooling of granitoids [*Lister and Snoke*, 1984; *Gapais*, 1989]. The diachronous origin of the two fabrics is also suggested by our data indicating distinct metamorphic grade associated with the S and C fabrics, respectively. The S fabric is defined by shape-preferred orientation of magmatic minerals such as large grains of white mica I and porphyroclasts of K-feldspar I and plagioclase (with unknown composition due to subsequent replacement by mixture of albite and white mica) which in the same fabric are overgrown/replaced by the newly formed plagioclase with anorthite component between 6 and 16 mol % (Figure 5). Furthermore, the S fabric is defined by shape-preferred orientation of recrystallized quartz aggregates dominated by grain boundary migration microstructure (Figures 2 and 10) that is typical for high temperature deformation >550°C [*Stipp et al.*, 2002; *Jeřábek et al.*, 2007]. Because of these relatively high temperatures and overprinting relations, the S fabric can be interpreted as magmatic-subsolidus formed during emplacement/cooling of the SASZ granitoids. In contrast, the C fabric is associated with albite-muscovite-chlorite-microcline assemblage with estimated P-T conditions of 100–400 MPa and 300–350°C (Figure 6). These temperatures are in a good agreement with sub-grain rotation recrystallization of quartz, which is observed in association with slip along the shear bands (Figures 2 and 11). The above temperature estimates comply with synkinematic cooling of the SASZ plutons from >550°C, marked by the S fabric, to 350°C, marked by the C fabric. However, the absence of transitional microstructures between the two end-member fabrics (S and C) suggests two distinct periods of deformation.

The texture analysis of recrystallized quartz from both S and C fabrics may also support the interpretation of two distinct periods of deformation as the two fabrics document kinematic criteria that are clearly dextral for shear bands but ambiguous for the S fabric. The basal $<a>$ dominated asymmetric quartz CPOs (Figure 10) obtained from the S fabric show both sinistral and dextral kinematics [cf. *Lister and Williams*, 1979; *Simpson and Schmid*, 1983]. Thus, although the asymmetry of quartz CPO is often used for kinematic interpretations [e.g., *Law et al.*, 1990], the results have to be considered with caution due to the effects of pure shear component [e.g., *Jeřábek et al.*, 2007] or heterogeneous distribution of strain and strain partitioning in the simple shear dominated deformation zones [*Krohe*, 1990; *Kilian et al.*, 2011]. Similarly, our results of quartz texture analysis suggest a complex evolution of the S fabric in comparison with relatively simple kinematics related to the C fabric.

5.1.1. Initiation of Shear Bands

Our P-T estimates for the C fabric show relatively low temperatures (300–350°C) and pressures (100–400 MPa) characteristic for the conditions of brittle-ductile mechanical transition in crustal rocks [e.g., *Peč et al.*, 2012]. Indeed, the studied rocks show intragranular microcracks identified in the quartz aggregates so that they crosscut the S fabric in an orientation close to the C bands (Figure 4). Moreover, the microcracks subparallel to C fabric are filled by minerals typical for shear bands, and therefore, they are interpreted as shear band precursors (Figures 4c and 7a). Microcracks have become frequently recognized as precursors of ductile shear zones affecting midcrustal granitoids [e.g., *Pennacchioni and Mancktelow*, 2007; *Fusseis and Handy*, 2008; *Mancktelow and Pennacchioni*, 2013] but also lower crustal rocks [*Menegon et al.*, 2013; *Okudaira et al.*, 2015]. The microcracking is typically explained by stress concentrations where the effective viscosity contrasts between weak and strong phases are high, e.g., at the tips of phyllosilicates [*Holyoke and Tullis*, 2006] or in material with the same composition but very different grain size [*Rybacki et al.*, 2014]. Similarly, the observed microcracks from SASZ are often associated with large white mica I grains elongated parallel to S and occurring within or in the vicinity of quartz aggregates (Figure 4a). The analysis of microcrack orientations show their dominant occurrence at an angle of 36° with respect to S followed by two subordinate peaks at 19° and 42° (Figure 4b). Microcracks with these orientations commonly show the C fabric matrix mineral infill (Figures 4c and 7a) while microcracks of other orientations are usually infill free. The relationship between orientation and infill suggests that the microcracks oriented at angles higher than 15° from S are suitably oriented for mineral precipitation and thus indicate an opening of microcracks formed at 36 ± 15° with respect to S (Figure 4b). Similar microcracks, as our initial microcracks, have been reported from deformation experiments of quartz aggregates [*Hirth and Tullis*, 1994] where the observed mode II cracks concentrated at ±15° with respect to main axial stress. Assuming that the observed microcracks in SASZ formed by similar mechanism the local orientation of main principal stress in the moment of cracking should be subparallel to the orientation of shear bands. On the other hand, in order to maintain the subsequent right-lateral shear displacement along the shear bands, the main principal stress vector should be at least
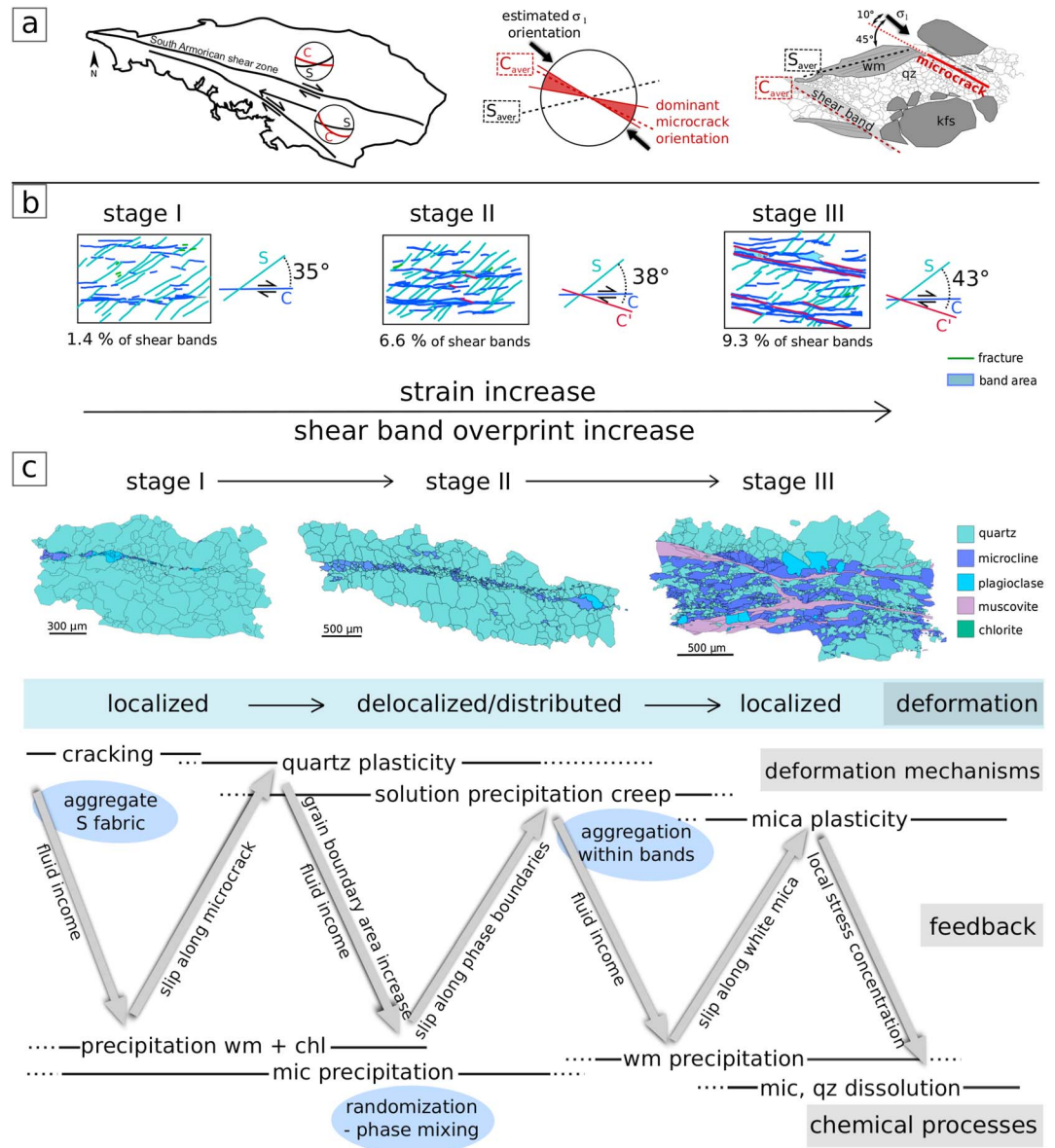
Figure 12. Synthesizing sketch of shear band evolution: (a) Orientation relationship of analyzed S-C fabrics with respect to two main branches of the SASZ and small-scale relations between S-C, microcracks (see Figure 3) and tentative orientation of the main principal stress σ_1. (b) Evolution of the S-C/C' fabric geometry with increasing strain and shear band overprint (see Figure 2). (c) Evolution of microstructure within shear bands as a result of interplay between various deformation mechanisms and chemical processes. The deformation along shear bands during the three stages occurs as localized or distributed/delocalized.

slightly clockwise rotated with respect to shear bands, i.e., NNW-SSE trending in geographic coordinates (Figure 12a). Assuming that the stress concentration and cracking are related to dislocation glide along the (001) plane of large white mica grains in S the highest Schmid factor of 0.5 corresponds to orientation of main principal stress at 45° with respect to S. Such slip would allow cracking at the tips of white mica [see, e.g., *Misra*, 2011] and also satisfies the observed dextral shear sense along shear bands (Figure 12a) suggesting that the cracks and shear bands may have followed a single kinematic condition. The opening microcracks and associated precipitation/crystallization of minerals lubricating the crack plane lead to the switch into viscous shearing along the microcracks. Thus, although the microcracking is initially an important mechanism for localization of deformation, its importance later decreases, with the deformation being accommodated by slip along thin shear bands [*Fusseis and Handy*, 2008].

5.1.2. Geometry of S-C/C′ Fabrics

It is interesting to note the changes in dihedral angle between the S and C/C′ fabrics toward higher degree of shear band overprint manifested mainly by the increasing proportion of shear band matrix at the expense of porphyroclasts in S (Figure 3). As summarized in Figure 12b, the average dihedral angle between S and C fabrics increases from 35° when the C bands are thin and isolated to 42° when the C bands increase their width and become interconnected. On the other hand, with further increase of shear band matrix proportion >13% the dihedral angle starts to decrease, and both fabrics become parallel/indistinguishable in the ultramylonite samples. The low dihedral angles for thin and isolated shear bands are in a good agreement with the most frequent orientation of microcracks indicating dihedral angles of 36°. This suggests that the initial orientation of shear bands is associated with relatively constant orientation of C with respect to S at ~35°. Similar initial dihedral angles have been previously reported by *Agard et al.* [2011] from Betic Cordilleras and *Gillam et al.* [2014] from New Zealand. The subsequent increase in dihedral angle is contrary to commonly observed decrease of the angle with increasing displacement along shear bands [e.g., *Berthé et al.*, 1979a; *Agard et al.*, 2011]. However, the inferred formation of C′ shear bands at low angles with respect to C shear bands and their spatial overlap [cf. *Blenkinsop and Treloar*, 1995] appears to be the likely explanation for the apparent increase in the S-C dihedral angle toward the stage III. The formation of C′ shear bands is manifested by deformation in the relay ramps connecting individual segments of C bands in stages II and III (see abc sketches in Figure 3d), which results in an increased scatter of the C fabric orientation (Figure 3d). The previously concluded relation between the low phase strength contrast and high phase strength contrast for the formation of C and C′ shear bands, respectively [*Holyoke and Tullis*, 2006], is in a good agreement with our observations documenting transition from distributed behavior (low contrast) to localized behavior (high contrast) toward the stage III, where C′ becomes prominent.

5.2. Mechanisms Related to Formation and Evolution of Shear Bands

Formation of shear bands at conditions of green schist to lower amphibolite facies is commonly associated with both brittle and crystal-plastic processes [e.g., *Passchier*, 1984]. In the original study of *Berthé et al.* [1979a, 1979b] from the South Armorican Shear Zone the formation of mylonites in the S fabric is associated with recrystallization of feldspars and quartz while the formation of shear bands (the C fabric) is associated with cataclasis and comminution of quartz, feldspars, and micas porphyroclasts. In their concept the concomitant development of both fabrics at ~450°C was interpreted as a consequence of progressive variation in the intensity of shear strain. In contrast, *Gapais and White* [1982] interpreted the formation of shear bands in association with dynamic recrystallization of quartz followed by softening associated with grain boundary sliding within the shear bands. These authors argued that the localization of deformation into shear bands occurs when the temperature decreases below the biotite isograd. Similarly, also in this work, the formation of shear bands is associated with relatively low temperatures 300–350°C (Figure 6). On the other hand, it is important to state that the below described evolution of shear bands is not related to temperature or pressure changes because (1) no major differences in assemblage or composition of shear band matrix minerals were detected amongst individual evolutionary stages and (2) the strike-slip character of SASZ prevents major changes in depth/pressure. The latter is supported by the similarity of our estimated pressures (100–400 MPa) for shear band assemblage in sample SB4 from the Questembert granite and its synkinematic emplacement to pressures of 100–200 MPa [*Tartèse and Boulvais*, 2010]. Thus, we assume that the S-C/C′ fabric and shear bands evolved during single kinematic continuum of dextral shear during cooling.

The evolution of shear bands in the SASZ was divided into three stages based on microstructural differences reflecting activation of different deformation mechanisms, while the switches between individual deformation mechanisms were controlled by the interplay and positive feedback between deformation and fluid-controlled chemical processes (Figure 12c). As discussed above the initiation stage I evolution of shear bands is associated with brittle deformation manifested by the presence of microcracks subparallel to later shear bands (Figure 12c, stage I). The microcracks opened pathways for fluids bringing in the elements to precipitate white mica, chlorite, microcline, and albite along the microcracks (Figure 7a). These newly precipitated phases acted as a lubricant facilitating the highly localized deformation and slip along the microcracks. Toward the stage II, slip along microcracks-induced crystal plasticity in the neighboring large quartz grains associated with the S fabric. Here the dislocation glide and activity of basal $<a>$ slip system led to formation of subgrains and recrystallized grains with considerably smaller grain size compared to the S fabric microstructure (Figure 11b). The lattice clockwise rotation of recrystallized quartz grains away from the orientation of parent grains is consistent with dextral sense of shearing along the shear bands (Figure 11b). Dynamic recrystallization of quartz

Table 2. Experimentally Derived Material Constants and Form of Flow Laws Used in Figure 13[a]

Mineral	Reference	A [MPa$^{-n}\times$s^{-1}]	Q [KJ $\times$ mol^{-1}]	n	Flow Law
quartz	*Paterson and Luan* [1990]	6.5×10^{-8}	135	3.1	$\varepsilon = A\times\sigma^n\times f_{(H_2O)}\times e^{-Q/RT}$
white mica	*Mares and Kronenberg* [1993]	4×10^{-20}	31	11	$\varepsilon = A\times\sigma^n\times e^{-Q/RT}$
white mica	*Mariani et al.* [2006]	$10^{7.23}$	270	1.13	$\varepsilon = A\times3^{-(n+1)/2}\times\sigma^n\times e^{-Q/RT}$
biotite	*Kronenberg et al.* [1990]	1.2×10^{-30}	51	18	$\varepsilon = A\times\sigma^n\times e^{-Q/RT}$

[a]In order to compare individual flow laws, the flow law for white mica of *Mariani et al.* [2006] relating shear strain rate and shear stress was rewritten into formula relating equivalent strain rate (ε) and equivalent stress (σ). The power law form of the flow law for white mica of *Mares and Kronenberg* [1993] was obtained by fitting their original data, except for the experiments performed at 2.3×10^{-4} s^{-1} in their strain rate-stepping series as these show unrealistic low stresses (see their Table 3). Fugacity coefficients (f$_{H_2O}$) for quartz flow law were used after *Tödheide* [1972]. A: material constant, *n*: stress exponent, Q: activation energy, R: Boltzmann constant, and T: temperature.

and associated increase in the density of grain boundaries facilitated an income of fluids and precipitation of microcline, whose appearance is characteristic for stage II of shear band evolution (Figure 12c, stage II). The precipitating microcline along the recrystallized quartz grain boundaries resulted in randomization of originally aggregate distribution of phases (Figure 9d), complete isolation of some quartz grains inside the shear bands (Figures 8a and 8b), and decrease in quartz grain size inside the shear bands (Figure 9b). Similar mechanism of phase mixing and reduction of quartz grain size by dissolution-replacement has been previously described from ultramylonitic shear zones in the Gran Paradiso by *Kilian et al.* [2011]. The continuing slip along shear bands at stage II is demonstrated by the loss and randomization of the originally host controlled CPO of the recrystallized quartz grains isolated within the microcline dominated matrix inside the shear bands (Figures 11c and 11d). At the same time, dynamic recrystallization of quartz at the boundaries between shear bands and quartz aggregates is still active and the above described positive feedback between quartz recrystallization, fluid infiltration, and microcline precipitation leads to progressive widening of the shear bands. Thus, distributed/delocalized deformation is characteristic for stage II. The observed replacement and precipitation inside the shear bands together with the lack of CPO and absence of dislocations in microcline (Figures 8c and 11d) suggest that the deformation at stage II is accommodated by dissolution-precipitation creep and some contribution of grain boundary sliding [*Wintsch and Yi*, 2002; *Menegon et al.*, 2008; *Fukuda et al.*, 2012]. The contribution of grain boundary sliding and associated cavitation [*Čadek*, 1988] allowed for income of fluids and precipitation of isolated white mica grains in dilatant sites (Figure 7c). As no substantial increase in white mica proportion was revealed by our thermodynamic modeling (Figure 6), it is likely that the newly formed white mica II reprecipitated/recrystallized from large grains of white mica I (see Figure 7c). At the same time, the grain boundary sliding along phase boundaries may have led to rearrangement of grains toward more aggregate phase distribution [*Hiraga et al.*, 2013] observed at the late stage II of shear band evolution (Figure 9d). Toward stage III, the isolated white mica grains with suitable orientation subparallel to shear bands started to interconnect partly as a result of crystal plasticity and the activation of the easy glide system along (001) planes. As the proportion of white mica in the studied samples (in S and C/C′ fabric) remains near constant (Figure 6), the reaction softening mechanism due to metamorphic transformation of K-feldspar to white mica [*Wintsch et al.*, 1995; *Wintsch and Yeh*, 2013] does not seem to be the key mechanism for the observed transition from stage II to stage III of shear band evolution. In contrast, it is the dispersion of reprecipitated white mica along the microcline-quartz boundaries together with its plasticity that could lead to their interconnection and thus accommodate the stage II to stage III switch (cf. Figures 7c and 7e). The interconnected white mica bands, typical for stage III (Figure 12c, stage III), crosscut and offset the previous and "frozen" microstructure of mixed quartz and microcline of stage II (Figure 7e) suggesting that the entire deformation within shear bands at stage III is accommodated by dislocation creep of white mica (Figure 11d). At the same time, this stage is characterized by highly localized deformation along white mica bands. Consequently, the slip along these bands leads to local stress concentrations along restraining bends inducing pressure solution of quartz and microcline occurring at the interfaces with white mica (Figure 8d) [see *Bukovská et al.*, 2015].

5.3. Rheological Implications of Shear Band Initiation

The above described four principal deformation mechanisms that are sequentially activated in the studied shear bands (Figure 12c) allowed us to evaluate rheology of these microscale shear zones and their strength contrast with respect to shear zone walls at individual stages of shear band evolution. For this purpose we applied experimentally derived flow laws (Table 2) for dislocation creep in quartz [*Paterson and Luan*, 1990]
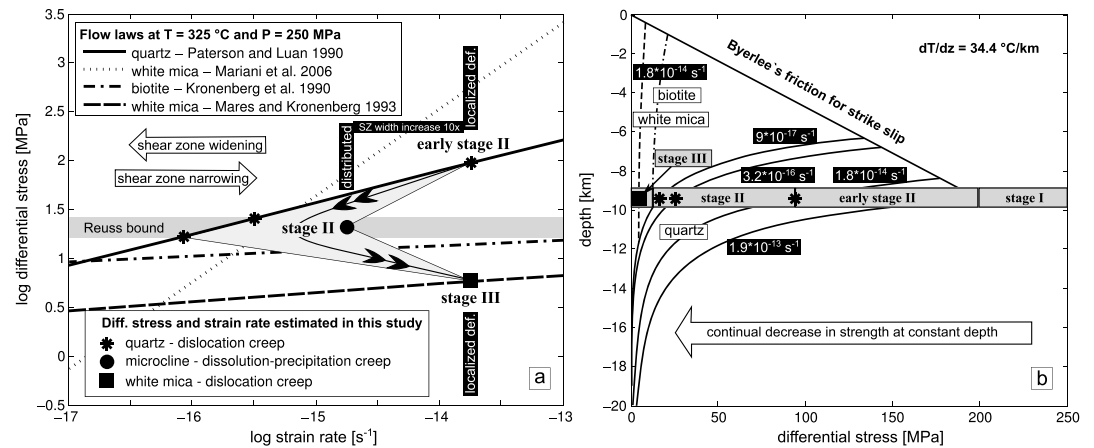
Figure 13. Rheological implications for brittle-plastic transition: (a) Changes in differential stress and strain rate during the evolution of shear bands revealed by the observed deformation microstructures and experimentally derived flow laws (Table 2) and its significance for shear band evolution. (b) Evolution of strength of the brittle-plastic transition recorded in the South Armorican Shear Zone during formation of shear bands. The strength curves are based on Byerlee's frictional envelope for strike-slip faults ($\mu = 0.85$, hydrostatic pore pressure, and σ_2 = mean stress) and on dislocation creep envelope derived from flow laws used in Figure 13b.

and micas [*Kronenberg et al.*, 1990; *Mares and Kronenberg*, 1993; *Mariani et al.*, 2006]. The temperatures and pressures used in rheological predictions were taken as average values from our P-T estimates, i.e., 250 MPa and 325°C (Figure 6). For the period of shear band evolution, these values are considered as near constant because of identical assemblage that was documented in all evolutionary stages (constant temperature) and strike-slip character of the SASZ (constant pressure). The differential stresses and strain rates calculated from the well-defined piezometric and creep relations for quartz were used to shed some light on the relatively unknown mechanical behavior of dissolution-precipitation creep in microcline and on the less well-constrained behavior of white mica. This goal was achieved by combining the mechanical data with observed changes in width of shear bands at individual stages (Figure 13a) under the assumption of at least temporarily constant displacement rate along the SASZ.

The identified sequence of deformation mechanisms from stage I to stage III of shear band evolution indicates transition from brittle to plastic behavior and continual decrease in strength of the SASZ (Figure 13b). Relatively high differential stresses are expected for initiation of shear bands via cracking at stage I. For our averaged P-T estimates, the yielding differential stress can be up to 250 MPa as reported from experiments on cracking of quartz single crystals [*Tarantola et al.*, 2012; *Diamond and Tarantola*, 2015]. Dynamic recrystallization of quartz via dislocation creep in the vicinity of microcracks and shear bands at stage II allowed us to evaluate stresses and strain rates by using the recrystallized quartz grains paleopiezometer of *Stipp and Tullis* [2003], corrected after *Holyoke and Kronenberg* [2010], and the flow law of *Paterson and Luan* [1990] (combination of flow laws and piezometers after *Boutonnet et al.* [2013]). For the early phases of stage II characterized by exclusive recrystallization of quartz due to slip along microcracks, the average grain size of 8 μm (Figure 11e; red grains in grain map in Figure 11b) indicates differential stress of 94 MPa and strain rate $1.8 \times 10^{-14}\,s^{-1}$ (Figure 13a). For later phases of stage II when recrystallization of quartz is accompanied by dissolution-precipitation creep of microcline, the average grain size of recrystallized quartz increases to 41 and 81 μm (Figure 11e), which corresponds to decrease in differential stresses to 26 and 17 MPa and strain rates to $3.2 \times 10^{-16}\,s^{-1}$ and $9 \times 10^{-17}\,s^{-1}$, respectively. The decrease in stresses and strain rates recorded by the recrystallized quartz layer at late phases of stage II is related not only to shear band widening but also to strain partitioning into the weaker dissolution-precipitation creep dominated layer of microcline (Figure 11c). This is because the widening itself, with approximately 10 times increase in shear band width (cf. Figures 11b and 11c), cannot alone account for 2 orders of magnitude decrease in strain rate recorded by quartz. Therefore, the stress decrease related to partitioning of deformation is the likely explanation for the observed relations. At the same time, assuming that both quartz and microcline layers deform at constant stress conditions (Reuss bound), the flow stresses for dissolution-precipitation creep of microcline correspond to quartz and range between 26 and 17 MPa (Figure 13a). Assuming constant displacement rate along SASZ and approximate 10 times increase in width of shear bands

at stage II can be translated into 10 times decrease in strain rate (Figure 13a). Thus, for given P-T conditions and stresses the dissolution-precipitation creep in microcline would accommodate deformation at strain rates of $1.8 \times 10^{-15} s^{-1}$ (Figure 13a). The stage III is characterized by localization of deformation into the white mica bands, which must have been accompanied by a substantial increase in strength contrast between the walls and the interior of shear bands, as the deformation in the walls of these newly established microshear zones ceased. Accordingly, this change implies a pronounced drop in stress needed to continue deformation in the internal part of shear bands represented by micaceous layers (e.g., Figure 12c). At the same time the observed localization of deformation at constant displacement rate condition suggests an increase in strain rate to at least the initial values of $1.8 \times 10^{-14} s^{-1}$ obtained for stage I. By plotting the existing mica flow laws into the stress and strain rate space, for the given temperatures and strain rates the substantial stress decrease is fully satisfied only by the dislocation creep flow law of *Mares and Kronenberg* [1993] showing 5.75 MPa at $1.8 \times 10^{-14} s^{-1}$ (Figure 13a).

5.4. Strength Evolution at Brittle-Ductile Transition

Strength of crustal rocks at brittle-plastic transition is controlled by their composition, interconnectivity of weak material, and preferred deformation mechanism [e.g., *Handy*, 1990; *Shea and Kronenberg*, 1993; *Kohlstedt et al.*, 1995]. When mechanical behavior of quartz is chosen to approximate the strength of crust, it can be concluded that ductile shearing accommodated by plasticity of quartz near the brittle-ductile transition requires the highest yielding stresses and therefore represents the strongest part of the continental crust [*Behr and Platt*, 2014]. However, when phyllosilicates are used instead, it is the frictional strength of faults that controls the crustal strength [*Mariani et al.*, 2006; *Wintsch and Yeh*, 2013]. The above described decrease of rock strength in SASZ implies that rheology of the brittle-ductile transition may be rather dynamic and not steady state in the initial stages of localization of deformation and that the crustal strength evolves in time and eventually can be reduced to extremely small values <10 MPa (Figure 13b). The observed decrease in strength is mainly due to switches in deformation mechanisms and changes in mineral phases accommodating deformation. Phase transformations thus appear as one of the key mechanisms for reaction softening and/or deviation from steady state behavior [*Stünitz and Tullis*, 2001; *Gueydan et al.*, 2003; *Oliot et al.*, 2010; *Goncalves et al.*, 2012; *Okudaira et al.*, 2015], especially at the brittle-ductile transition where sufficient permeability and income of acidic meteoric water may lead to substantial increase in the white mica content [*Wintsch et al.*, 1995; *Wintsch and Yeh*, 2013]. On the other hand, as demonstrated in this work it is also the crystal plastic and brittle processes in combination with precipitation/neocrystallization that lead to efficient phase mixing and formation of relatively weak matrix bands. In addition, the documented evolution in these microscale shear zones indicate that shear zones can both become wider or narrower during the same deformation event, and therefore, the constant stress and steady state approach used for estimates on width of major crustal shear zones [*Platt and Behr*, 2011] may not be applicable in evolving shear zones.

6. Conclusions

Formation and evolution of S-C/C' fabrics in the South Armorican Shear Zone have been evaluated by detailed microstructural study including determination of mineral chemistry, quantitative microstructural analysis, transmission electron microscopy, and textural analysis by EBSD method. Our observations suggest that the two fabrics formed at distinct P-T conditions indicating magmatic-subsolidus conditions >550°C for the S fabric and 300–350°C at 100–400 MPa for the C fabric/shear bands. The evolving microstructure within shear bands revealed important switches in deformation mechanisms related to positive feedbacks between deformation and chemical processes and imposing mechanical constraints on evolution of the brittle-ductile transition. Three stages of shear band evolution were identified. Stage I is associated with initiation of shear bands via formation of microcracks acting as precursors for shear bands. For the estimated P-T conditions, the yielding differential stresses for cracking can be up to 250 MPa. The initial phases of stage II are associated with localized slip along microcracks which triggered subgrain rotation recrystallization via dislocation creep in neighboring quartz at relatively high differential stresses of 94 MPa and strain rate $1.8 \times 10^{-14} s^{-1}$. The recrystallization facilitated income of fluids and precipitation of microcline along quartz grain boundaries, which resulted in phase mixing and widening of shear bands. The slip along shear bands at later phases of stage II was mainly accommodated by dissolution-precipitation creep of microcline with some contribution of grain boundary sliding. Coeval recrystallization of quartz shows increase in grain size/decrease in stress

which by using the isostress Reuss bound behavior allowed us to quantify stresses for dissolution-precipitation creep in the range of 17–26 MPa accommodating deformation at strain rate $1.8 \times 10^{-15}\,\text{s}^{-1}$. Stage III is characterized by reprecipitation and interconnection of white mica grains resulting into localized slip along white mica bands. The deformation in white mica is accommodated by dislocation creep at strain rate $1.8 \times 10^{-14}\,\text{s}^{-1}$ and stress 5.75 MPa. These mechanical data point to nonsteady state evolution of the brittle-ductile transition in the South Armorican Shear Zone characterized by major weakening to strengths lower than 10 MPa.

References

Agard, P., R. Augier, and P. Monié (2011), Shear band formation and strain localization on a regional scale: Evidence from anisotropic rocks below a major detachment (Betic Cordilleras, Spain), *J. Struct. Geol.*, *33*, 114–131.

Auzanneau, E., M. W. Schmidt, D. Vielzeuf, and J. A. D. Connolly (2010), Titanium in phengite: A geobarometer for high temperature eclogites, *Contrib. Mineral. Petrol.*, *159*, 1–24.

Ballèvre, M., V. Bosse, C. Ducassou, and P. Pitra (2009), Palaeozoic history of the Armorican Massif: Models for the tectonic evolution of the suture zones, *C. R. Geosci.*, *341*(2), 174–201.

Behr, W. M., and J. P. Platt (2014), Brittle faults are weak, yet the ductile middle crust is strong: Implications for lithospheric mechanics, *Geophys. Res. Lett.*, *41*, 8067–8075, doi:10.1002/2014GL061349.

Bercovici, D. (2003), The generation of plate tectonics from mantle convection, *Earth Planet. Sci. Lett.*, *205*(3), 107–121.

Berthé, D., P. Choukroune, and P. Jegouzo (1979a), Orthogneiss, mylonite and non coaxial deformation of granites: The example of the South Armorican Shear Zone, *J. Struct. Geol.*, *1*, 31–42.

Berthé, D., P. Choukroune, and D. Gapais (1979b), Orientations préférentielles du quartz et orthogneissification progressive en régime cisaillant: L'exemple du cisaillement sud-armoricain, *Bull. Mineral.*, *102*, 265–272.

Blenkinsop, T. G., and P. J. Treloar (1995), Geometry, classification and kinematics of S-C and S-C' fabrics in the Mushandike area, Zimbabwe, *J. Struct. Geol.*, *17*(3), 397–408.

Boutonnet, E., P. H. Leloup, C. Sassier, V. Gardien, and Y. Ricard (2013), Ductile strain rate measurements document long-term strain localization in the continental crust, *Geology*, *41*(8), 819–822.

Broussolle, A., et al. (2015), P–T–t–D record of crustal-scale horizontal flow and magma-assisted doming in the SW Mongolian Altai, *J. Metamorph. Geol.*, *33*(4), 359–383.

Bukovská, Z., P. Jeřábek, O. Lexa, J. Konopásek, M. Janák, and J. Košler (2013), Kinematically unrelated C—S fabrics: An example of extensional shear band cleavage from the Veporic Unit (Western Carpathians), *Geol. Carpathica*, *64*(2), 103–116.

Bukovská, Z., R. Wirth, and L. F. G. Morales (2015), Pressure solution in rocks: Focused ion beam/transmission electron microscopy study on orthogneiss from South Armorican Shear Zone, France, *Contrib. Mineral. Petrol.*, *170*(3), 1–13.

Čadek, J. (1988), *Creep in Metallic Materials*, 372 pp., Elsevier, Amsterdam.

Chopin, F., et al. (2012), Crustal influx, indentation, ductile thinning and gravity redistribution in a continental wedge: Building a Moldanubian mantled gneiss dome with underthrust Saxothuringian material (European Variscan belt), *Tectonics*, *31*, TC1013, doi:10.1029/2011TC002951.

Coggon, R., and T. Holland (2002), Mixing properties of phengitic micas and revised garnet-phengite thermobarometers, *J. Metamorph. Geol.*, *20*, 683–96.

Connolly, J. A. D. (2005), Computation of phase equilibria by linear programming: A tool for geodynamic modeling and its application to subduction zone decarbonation, *Earth Planet. Sci. Lett.*, *236*(1), 524–541.

Crider, J. G., and D. C. Peacock (2004), Initiation of brittle faults in the upper crust: A review of field observations, *J. Struct. Geol.*, *26*(4), 691–707.

Diamond, L. W., and A. Tarantola (2015), Interpretation of fluid inclusions in quartz deformed by weak ductile shearing: Reconstruction of differential stress magnitudes and pre-deformation fluid properties, *Earth Planet. Sci. Lett.*, *417*, 107–119.

Fukuda, J. I., T. Okudaira, T. Satsukawa, and K. Michibayashi (2012), Solution–precipitation of K-feldspar in deformed granitoids and its relationship to the distribution of water, *Tectonophysics*, *532*, 175–185.

Fusseis, F., and M. Handy (2008), Micromechanisms of shear zone propagation at the brittle-viscous transition, *J. Struct. Geol.*, *30*, 1242–1253.

Gapais, D. (1989), Shear structures within deformed granites: Mechanical and thermal indicators, *Geology*, *17*, 1144–1147.

Gapais, D., and S. H. White (1982), Ductile shear bands in a naturally deformed quartzite, *Textures Microstruct.*, *5*, 1–17.

Gillam, B. G., T. A. Little, E. Smith, and V. G. Toy (2014), Reprint of Extensional shear band development on the outer margin of the Alpine mylonite zone, Tatare Stream, Southern Alps, New Zealand, *J. Struct. Geol.*, *64*, 115–134.

Goncalves, P., E. Oliot, D. Marquer, and J. A. D. Connolly (2012), Role of chemical processes on shear zone formation: An example from the Grimsel metagranodiorite (Aar massif, Central Alps), *J. Metamorph. Geol.*, *30*(7), 703–722.

Gueydan, F., Y. M. Leroy, L. Jolivet, and P. Agard (2003), Analysis of continental midcrustal strain localization induced by microfracturing and reaction-softening, *J. Geophys. Res.*, *108*(B2), 2064, doi:10.1029/2001JB000611.

Gueydan, F., Y. M. Leroy, and L. Jolivet (2004), Mechanics of low-angle extensional shear zones at the brittle-ductile transition, *J. Geophys. Res.*, *109*, B12407, doi:10.1029/2003JB002806.

Gumiaux, C., D. Gapais, J. P. Brun, J. Chantraine, and G. Ruffet (2004), Tectonic history of the Hercynian Armorican shear belt (Brittany, France), *Geodinamica Acta*, *17*(4), 289–307.

Handy, M. (1990), The solid-state flow of polymineralic rocks, *J. Geophys. Res.*, *95*(B6), 8647–8661, doi:10.1029/JB095iB06p08647.

Hielscher, R., and H. Schaeben (2008), A novel pole figure inversion method: Specification of the MTEX algorithm, *J. Appl. Crystallogr.*, *41*(6), 1024–1037.

Hiraga, T., T. Miyazaki, H. Yoshida, and M. E. Zimmerman (2013), Comparison of microstructures in superplastically deformed synthetic materials and natural mylonites: Mineral aggregation via grain boundary sliding, *Geology*, *41*(9), 959–962.

Hirth, G., and J. Tullis (1994), The brittle-plastic transition in experimentally deformed quartz aggregates, *J. Geophys. Res.*, *99*(B6), 11,731–11,747, doi:10.1029/93JB02873.

Holland, T., and R. Powell (1998), An internally consistent thermodynamic data set for phases of petrological interest, *J. Metamorph. Geol.*, *16*, 309–43.

Holland, T., J. Baker, and R. Powell (1998), Mixing properties and activity-composition relationships of chlorites in the system MgO-FeO-Al$_2$O$_3$-SiO$_2$-H$_2$O, *Eur. J. Mineral.*, *10*, 395–406.

Holyoke, C. W., and A. K. Kronenberg (2010), Accurate differential stress measurement using the molten salt cell and solid salt assemblies in the Griggs apparatus with applications to strength, piezometers and rheology, *Tectonophysics*, *494*(1), 17–31.

Holyoke, C. W., and J. Tullis (2006), Mechanisms of weak phase interconnection and the effects of phase strength contrast on fabric development, *J. Struct. Geol.*, *28*(4), 621–640.

Janoušek, V., C. M. Farrow, and V. Erban (2006), Interpretation of whole-rock geochemical data in igneous geochemistry: Introducing Geochemical Data Toolkit (GCDkit), *J. Petrol.*, *47*, 1255–1259.

Jeřábek, P., H. Stünitz, R. Heilbronner, O. Lexa, and K. Schulmann (2007), Microstructural-deformation record of an orogen-parallel extension in the Vepor Unit, West Carpathians, *J. Struct. Geol.*, *29*(11), 1722–1743.

Jiang, Y. D., et al. (2015), Juxtaposition of Barrovian and migmatite domains in the Chinese Altai: A result of crustal thickening followed by doming of partially molten lower crust, *J. Metamorph. Geol.*, *33*(1), 45–70.

Karato, S. (1983), Importance of anelasticity in the interpretation of seismic tomography, *Geophys. Res. Lett.*, *20*(15), 1623–1626, doi:10.1029/93GL01767.

Keller, L. M., R. Abart, H. Stünitz, and C. De Capitani (2004), Deformation, mass transfer and mineral reactions in an eclogite facies shear zone in a polymetamorphic metapelite (Monte Rosa nappe, western Alps), *J. Metamorph. Geol.*, *22*(2), 97–118.

Kilian, R., R. Heilbronner, and H. Stünitz (2011), Quartz grain size reduction in a granitoid rock and the transition from dislocation to diffusion creep, *J. Struct. Geol.*, *33*, 1265–1284.

Knipe, R. J., and R. P. Wintsch (1985), Heterogeneous deformation, foliation development, and metamorphic processes in a polyphase mylonite, in *Metamorphic Reactions*, pp. 180–210, Springer, New York.

Kohlstedt, D. L., B. Evans, and S. J. Mackwell (1995), Strength of the lithosphere: Constraints imposed by laboratory experiments, *J. Geophys. Res.*, *100*, 17–587, doi:10.1029/95JB01460.

Kretz, R. (1969), On the spatial distribution of crystals in rocks, *Lithos*, *2*, 39–66.

Kretz, R. (1994), *Metamorphic Crystallization*, Wiley, Chichester and New York.

Krohe, A. (1990), Local variations in quartz [*c*]-axis orientations in non-coaxial regimes and their significance for the mechanics of S-C fabrics, *J. Struct. Geol.*, *12*(8), 995–1004.

Kronenberg, A. K., S. H. Kirby, and J. Pinkston (1990), Basal slip and mechanical anisotropy of biotite, *J. Geophys. Res.*, *95*(B12), 19,257–19,278, doi:10.1029/JB095iB12p19257.

Law, R. D., S. M. Schmid, and J. Wheeler (1990), Simple shear deformation and quartz crystallographic fabrics: A possible natural example from the Torridon area of NW Scotland, *J. Struct. Geol.*, *12*(1), 29–45.

Lexa, O. (2003), Numerical approach in structural and microstructural analyses, PhD thesis, p. 138, Charles Univ., Prague.

Lister, G. S., and A. W. Snoke (1984), S-C Mylonites, *J. Struct. Geol.*, *6*(6), 617–638.

Lister, G. S., and P. F. Williams (1979), The partitioning of deformation in flowing rock masses, *Tectonophysics*, *92*(1), 1–33.

Lloyd, G. E. (2004), Microstructural evolution in a mylonitic quartz simple shear zone: The significant roles of dauphine twinning and misorientation, *Geol. Soc. London, Spec. Publ.*, *224*(1), 39–61.

Mancktelow, N. S., and G. Pennacchioni (2013), Late magmatic healed fractures in granitoids and their influence on subsequent solid-state deformation, *J. Struct. Geol.*, *57*, 81–96.

Mariani, E., K. H. Brodie, and E. H. Rutter (2006), Experimental deformation of muscovite shear zones at high temperatures under hydrothermal conditions and the strength of phyllosilicate-bearing faults in nature, *J. Struct. Geol.*, *28*(9), 1569–1587.

Mares, V. M., and A. K. Kronenberg (1993), Experimental deformation of muscovite, *J. Struct. Geol.*, *15*(9), 1061–1075.

Means, W. D. (1995), Shear zones and rock history, *Tectonophysics*, *247*, 157–160.

Menegon, L., G. Pennacchioni, R. Heilbronner, and L. Pittarello (2008), Evolution of quartz microstructure and *c*-axis crystallographic preferred orientation within ductilely deformed granitoids (Arolla unit, Western Alps), *J. Struct. Geol.*, *30*(11), 1332–1347.

Menegon, L., H. Stünitz, P. Nasipuri, R. Heilbronner, and H. Svahnberg (2013), Transition from fracturing to viscous flow in granulite facies perthitic feldspar (Lofoten, Norway), *J. Struct. Geol.*, *48*, 95–112.

Miller, C. F., E. F. Stoddard, L. J. Bradfish, and W. A. Dollase (1981), Composition of plutonic muscovite: Genetic implications, *Can. Mineral.*, *19*, 25–34.

Misra, S. (2011), Deformation localization at the tips of shear fractures: An analytical approach, *Tectonophysics*, *503*, 182–187.

Montési, L. G. (2007), A constitutive model for layer development in shear zones near the brittle-ductile transition, *Geophys. Res. Lett.*, *34*, L08307, doi:10.1029/2007GL029250.

Neumann, B. (2000), Texture development of recrystallised quartz polycrystals unravelled by orientation and misorientation characteristics, *J. Struct. Geol.*, *22*(11), 1695–1711.

Newton, R. C., T. V. Charlu, and O. J. Kleppa (1980), Thermochemistry of the high structural state plagioclases, *Geochim. Cosmochim. Acta*, *44*, 933–41.

Okudaira, T., T. Takeshita, I. Hara, and I. J. Ando (1995), A new estimate of the conditions for transition from basal $<a>$ to prism [c] slip in naturally deformed quartz, *Tectonophysics*, *250*(1), 31–46.

Okudaira, T., P. Jeřábek, H. Stünitz, and F. Fusseis (2015), High-temperature fracturing and subsequent grain-size-sensitive creep in lower crustal gabbros: Evidence for coseismic loading followed by creep during decaying stress in the lower crust?, *J. Geophys. Res. Solid Earth*, *120*, 3119–3141, doi:10.1002/2014JB011708.

Oliot, E., P. Goncalves, and D. Marquer (2010), Role of plagioclase and reaction softening in a metagranite shear zone at mid-crustal conditions (Gotthard Massif, Swiss Central Alps), *J. Metamorph. Geol.*, *28*(8), 849–871.

Oliot, E., P. Goncalves, K. Schulmann, D. Marquer, and O. Lexa (2014), Mid-crustal shear zone formation in granitic rocks: Constraints from quantitative textural and crystallographic preferred orientation analyses, *Tectonophysics*, *612–613*, 63–80.

Passchier, C. W. (1984), The generation of ductile and brittle shear bands in a low-angle mylonite zone, *J. Struct. Geol.*, *6*(3), 273–281.

Passchier, C. W. (1991), Geometric constraints on the development of shear bands in rocks, *Geol. Mijnbouw*, *70*, 203–211.

Paterson, M. S., and F. C. Luan (1990), Quartzite rheology under geological conditions, *Geol. Soc. London, Spec. Publ.*, *54*(1), 299–307.

Peč, M., H. Stünitz, and R. Heilbronner (2012), Semi-brittle deformation of granitoid gouges in shear experiments at elevated pressures and temperatures, *J. Struct. Geol.*, *38*, 200–221.

Pennacchioni, G., and N. S. Mancktelow (2007), Nucleation and initial growth of a shear zone network within compositionally and structurally heterogeneous granitoids under amphibolite facies conditions, *J. Struct. Geol.*, *29*, 1757–1780.

Platt, J. P. (1984), Secondary cleavages in ductile shear zones, *J. Struct. Geol.*, *6*(4), 439–442.

Platt, J. P., and W. M. Behr (2011), Grain size evolution in ductile shear zones: Implications for strain localization and the strength of the lithosphere, *J. Struct. Geol.*, *33*(4), 537–550.

Platt, J. P., and R. L. M. Vissers (1980), Extensional structures in anisotropic rocks, *J. Struct. Geol.*, *2*(4), 397–410.

Powell, R., and T. Holland (1999), Relating formulations of the thermodynamics of mineral solid solutions: Activity modeling of pyroxenes, amphiboles, and micas, *Am. Mineral.*, *84*, 1–14.

Ranalli, G. (1987), *Rheology of the Earth*, Allen & Unwin, Boston, Mass.

Rutter, E. H. (1999), On the relationship between the formation of shear zones and the form of the flow law for rocks undergoing dynamic recrystallization, *Tectonophysics*, *303*(1), 147–158.

Rutter, E. H., R. E. Holdsworth, and R. J. Knipe (2001), The nature and tectonic significance of fault-zone weakening: An introduction, *Geol. Soc. London, Spec. Publ.*, *186*(1), 1–11.

Rybacki, E., L. F. G. Morales, M. Naumann, and G. Dresen (2014), Strain localization during high temperature creep of marble: The effect of inclusions, *Tectonophysics*, *634*, 182–197, doi:10.1016/j.tecto.2014.07.032.

Schmid, S. M. (1982), Microfabric studies as indicators of deformation mechanisms and flow laws operative in mountain building, in *Mountain Building Processes*, edited by K. J. Hsii, pp. 95–110, Academic Press, London.

Schulmann, K., B. Mlčoch, and R. Melka (1996), High-temperature microstructures and rheology of deformed granite, Erzgebirge, Bohemian Massif, *J. Struct. Geol.*, *18*(6), 719–733.

Shea, W. T., and A. K. Kronenberg (1993), Strength and anisotropy of foliated rocks with varied mica contents, *J. Struct. Geol.*, *15*(9), 1097–1121.

Simpson, C., and S. M. Schmid (1983), An evaluation of criteria to deduce the sense of movement in sheared rocks, *Geol. Soc. Am. Bull.*, *94*(11), 1281–1288.

Stipp, M., and J. Tullis (2003), The recrystallized grain size piezometer for quartz, *Geophys. Res. Lett.*, *30*(21), 2088, doi:10.1029/2003GL018444.

Stipp, M., H. Stünitz, R. Heilbronner, and S. M. Schmid (2002), The eastern Tonale fault zone: A "natural laboratory" for crystal plastic deformation of quartz over a temperature range from 250 to 700 C, *J. Struct. Geol.*, *24*(12), 1861–1884.

Stünitz, H., and J. Tullis (2001), Weakening and strain localization produced by syn-deformational reaction of plagioclase, *Int. J. Earth Sci.*, *90*, 136–148.

Tarantola, A., L. W. Diamond, H. Stünitz, A. Thust, and M. Peč (2012), Modification of fluid inclusions in quartz by deviatoric stress. III: Influence of principal stresses on inclusion density and orientation, *Contrib. Mineral. Petrol.*, *164*(3), 537–550.

Tartèse, R., and P. Boulvais (2010), Differentiation of peraluminous leucogranites "en route" to the surface, *Lithos*, *114*, 353–368.

Tartèse, R., M. Poujol, G. Ruffet, P. Boulvais, P. Yamato, and J. Košler (2011), New U-Pb zircon and 40 Ar/39 Ar muscovite age constraints on the emplacement of the Lizio syn-tectonic granite (Armorican Massif, France), *C. R. Geosci.*, *343*(7), 443–453.

Tartèse, R., P. Boulvais, M. Poujol, T. Chevalier, J. L. Paquette, T. R. Ireland, and E. Deloule (2012), Mylonites of the South Armorican Shear Zone: Insights for crustal-scale fluid flow and water–rock interaction processes, *J. Geodyn.*, *56*, 86–107.

Tödheide, K. (1972), Water at high temperature and pressure, in *Water: A Comprehensive Treatise*, vol. 1, edited by F. Franks, pp. 463–514, Plenum Press, New York.

White, S. H., S. E. Burrows, J. Carreras, N. D. Shaw, and F. J. Humpreys (1980), On mylonites in ductile shear zones, *J. Struct. Geol.*, *2*, 175–187.

Wilks, K. R., and N. L. Carter (1990), Rheology of some continental lower crustal rocks, *Tectonophysics*, *182*(1), 57–77.

Wintsch, R. P., and M. W. Yeh (2013), Oscillating brittle and viscous behavior through the earthquake cycle in the Red River Shear Zone: Monitoring flips between reaction and textural softening and hardening, *Tectonophysics*, *587*, 46–62.

Wintsch, R. P., and K. Yi (2002), Dissolution and replacement creep: A significant deformation mechanism in mid-crustal rocks, *J. Struct. Geol.*, *24*(6), 1179–1193.

Wintsch, R. P., R. Christoffersen, and A. K. Kronenberg (1995), Fluid-rock reaction weakening of fault zones, *J. Geophys. Res.*, *100*(B7), 13,021–13,032, doi:10.1029/94JB02622.

Wirth, R. (2009), Focused Ion Beam (FIB) combined with SEM and TEM: Advanced analytical tools for studies of chemical composition, microstructure and crystal structure in geomaterials on a nanometre scale, *Chem. Geol.*, *261*(3), 217–229.